Micro and Nanostructures 216 (2026) 208709

Contents lists available at ScienceDirect

Micro and Nanostructures

journal homepage: www.journals.elsevier.com/micro-and-nanostructures

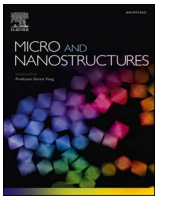

Crystal structure, morphology, magnetic, electrical, and dielectric characterization of amphoteric Yb_2O_3-modified lead-free $BaTiO_3$ perovskite

Yassine Slimani [a,*], Bayram Ünal [b], Abdulhadi Baykal [c], Atul Thakur [d,e]

[a] Department of Biophysics, Institute for Research and Medical Consultations (IRMC), Imam Abdulrahman Bin Faisal University, P.O. Box 1982, Dammam, 31441, Saudi Arabia
[b] Department of Electrical and Electronics Engineering, Faculty of Engineering and Architecture, İstanbul Gelisim University, Avcılar, Istanbul, Türkiye
[c] Food Engineering Department, Faculty of Engineering, Istanbul Aydin University, Florya, 34295, Istanbul, Türkiye
[d] Division of Research and Development, Lovely Professional University, Jalandhar, Punjab, 144411, India
[e] Centre of Excellence in Nanotechnology, Lovely Professional University, Phagwara, Punjab 144411, India

ARTICLE INFO

Keywords:
Lead-free $BaTiO_3$
Composite ceramic
Amphoteric
Dielectric properties
Conduction mechanism
Nyquist plots

ABSTRACT

Large-scale perovskite applications require a lead-free matrix with tolerable properties. Rare earth doping can be an effective way to achieve an enhanced performance. While previous studies have primarily focused on low rare-earth doping levels, research into reaching the maximum solubility limit of the guest rare earth into the perovskite host is still notably sparse. This work investigates the structural, morphological, magnetic, electrical, and dielectric properties of lead-free $BaTiO_3$ (BTO) perovskite ceramic modified with high weight fractions (2–20 wt%) of amphoteric Yb_2O_3. X-ray diffraction (XRD) analysis revealed a composite-like microstructure where Yb_2O_3 persists as a separate phase across all concentrations, while the host lattice exhibited an oscillatory volume response, highlighting the amphoteric transition of Yb^{3+} ions between A and B sites. Scanning electron microscopy and energy-dispersive X-ray spectroscopy (SEM/EDX) mapping revealed typical quasi-spherical and polyhedral BTO grains alongside irregular Yb_2O_3 precipitates. The magnetization versus applied magnetic field (*M(H)*) analysis showed hysteresis loops, reflecting ferromagnetic behavior of the samples, likely governed by the bound magnetic polaron (BMP) model. The electrical and dielectric properties of $BaTiO_3/xYb_2O_3$ ceramics were also systematically examined over a temperature range from 20 °C to 120 °C. AC conductivity exhibits characteristic dispersive behavior tracking universal Jonscher power law (UJPL), confirming a thermally activated hopping conduction explained by the correlated barrier hopping (CBH) model. The frequency exponent ($0 \leq s \leq 1$) reduces with rising temperature, indicating enhanced charge-carrier mobility. DC conductivity obeys Arrhenius performance, with the activation energy greatly dependent on additive concentration; moderate Yb_2O_3 contents (2–10 wt%) improve charge transport, while higher concentrations stimulate defect-induced carrier trapping. A pronounced reduction in dielectric constant (from ~1500 to ~5–20) is observed due to the construction of a composite microstructure and dominance of ferroelectric polarization. In the meantime, the dielectric loss and dissipation factor are significantly diminished. Impedance analysis reveals non-Debye relaxation, dominated by grain-boundary and interfacial effects. These findings demonstrate that Yb_2O_3 modification and composite formation provide an

* Corresponding author.
E-mail addresses: yaslimani@iau.edu.sa, slimaniyassine18@gmail.com (Y. Slimani).

https://doi.org/10.1016/j.micrna.2026.208709
Received 7 February 2026; Received in revised form 1 April 2026; Accepted 19 April 2026
Available online 19 April 2026

effective strategy for tailoring the electrical performance of $BaTiO_3$ ceramics for advanced dielectric applications.

1. Introduction

During the last decades, materials research has been oriented to focus on the design of advanced functional materials using compositional, defect, and heterostructure engineering strategies. Regulated doping and/or phase engineering can alter the structural features and electronic structure of materials, allowing for significant advances in catalytic, optical, electronic, dielectric, and corrosion-resistant capabilities [1–6]. Within this broader context of functional optimization, over the last few years, numerous nations have implemented restricted regulations on electronics that contain lead oxide-based materials to safeguard public health and minimize ecological damage [7]. Therefore, the replacement of conventional lead-based ceramics with eco-friendly lead-free alternatives is nowadays an important long-term goal. In this frame, perovskite-based ceramics, with the general formula ABO_3, represent a large and interesting class of ferroelectric ceramics, characterized by unique properties such as good dielectric properties and excellent chemical stability [8]. These important properties make perovskite compounds good alternatives for lead oxide-based ceramics. In addition, the drive towards miniaturization and increased applicability in small electrical structures requires special attention to a robust design matrix.

Among perovskite compounds, barium titanate ($BaTiO_3$, BTO) stands out as one of the most viable alternatives to lead-containing materials. This attention stems from its exceptional dielectric constant, ferroelectric behavior, nonlinear optical coefficients, and spontaneous polarization, making it efficient for microelectronics, ferroelectric, and optoelectronics applications [9]. BTO is frequently utilized to fabricate a variety of devices such as multilayer ceramic capacitors (MLCC), piezoelectric devices, ultrasonic transducers, high-density optical data storage, positive temperature coefficient resistors, etc. [10–13]. The crystalline structure of BTO is temperature-dependent, transitioning through various phases, including orthorhombic, tetragonal, hexagonal, and cubic systems. At room temperature, the tetragonal crystal system exhibits the highest stability [14]. While it is highly versatile, the intrinsic physical characteristics of pristine $BaTiO_3$ still show inferior performance compared to conventional lead-based ceramic materials. To address this, several approaches, including chemical doping, forming composites, grain size tuning, surface modification, etc., have been adopted to enhance the performance of BTO compound [15–20]. The versatility of BTO stems from its strong perovskite structure, which holds a high degree of flexibility. This lattice can accommodate a wide variety of guest cations through A-site or B-site substitution. Many cation dopants have been employed to modulate the electrical traits of the material [21]. In particular, rare-earth oxide (REOs) elements were reported to stabilize BTO and provide a boosted dielectric constant and low dielectric loss [22]. It is widely reported that small amounts of RE ions, ranging from large ionic radius (such as La^{3+}, Pr^{3+}, Nd^{3+}, etc.) to small ionic radius (e.g., Er^{3+}, Yb^{3+}), effectively suppress grain growth through grain-boundary pinning mechanisms [23]. In addition, some of REOs can act as aliovalent dopants (due to their different charge from the ions of the host BTO), leading to the formation of defects, achieving colossal permittivity with low loss, and providing outstanding high-temperature stability, which are essential for miniaturized electronics [24, 25]. REOs also lead to improving the lifespan and reliability of electric devices, namely MLCCs, by preventing the migration of oxygen vacancies, which would otherwise lead to insulation failure [25–27].

Heavy ions such as Yb^{3+} ions have ionic radii intermediate between Ba^{2+} (A-site) and Ti^{4+} (B-site). Eventually, they can act as donors when lodged into the A-sites and as acceptors when incorporating in the B-sites [26]. This amphoteric behavior led to tailoring the electrical properties of BTO [23,28]. Specifically, the incorporation of a small amount of Yb_2O_3 has been identified as an effective way for grain refinement, due to the lower solubility of the small Yb^{3+} ion compared to larger RE ions. Yb_2O_3 also has a tendency to segregate more readily at the grain boundaries, providing a strong physical barrier against grain migration [26]. Moreover, the amphoteric nature of Yb^{3+} enables it to lodge either in the A or B sublattices of BTO. This effect effectively disrupts long-range ferroelectric order, leading to an increase in the dielectric properties of BTO [29]. Several investigations have been performed on BTO modified with REOs. For instance, J. H. Park et al. reported the effects of 1 mol% of MgO and different 1 mol% of REOs, including Y_2O_3, Dy_2O_3, and Yb_2O_3, on the structural and electrical characteristics of BTO compound [26]. Their results showed a single tetragonal phase obtained for pure BTO, Y_2O_3–MgO co-modified BTO, and Dy_2O_3–MgO co-modified BTO samples. Nevertheless, a pseudo-cubic structure and secondary phases were detected in MgO-Yb_2O_3 co-modified BTO samples. The authors ascribed this effect to the fact that the solubility limit of Yb^{3+} ions in the BTO system was achieved. Importantly, among the different samples, MgO-Yb_2O_3 co-modified BTO samples demonstrated good performance for MLCCs' applications. G. Yao et al. showed that Yb^{3+} ions have a leading role in shifting the Curie temperature (T_c) of BTO [30]. Y.H. Song et al. reported the positive effects of 1 mol % of REOs, namely Ho_2O_3, Yb_2O_3, and Er_2O_3, on enhancing the temperature stability, reducing dielectric loss, controlling grain growth, and shifting T_c for electronic applications such as X8R capacitors [31]. Soo Kyong Jo et al. examined the impact of multi-doping of REOs (RE = La, Yb, Ho, Nd, and Sm) on the performance of BTO. The authors concluded that the dielectric performance and microstructural evolution of BTO are heavily influenced by unit-cell volume. The latter is linked to the specific lattice sites occupied by RE ions and their respective ionic radii [32].

While previous studies have extensively emphasized the low-level dopant concentrations of amphoteric Yb_2O_3, there is a lack of systematic data regarding the structural and functional evolution in the high-loading regime. This work aims to systematically investigate the effect of high concentration of Yb_2O_3 additions (ranging from 2 wt% to 20 wt%), leading to the formation of $BaTiO_3$/Yb_2O_3 ceramic composites, on the phase evolution, microstructural morphology, magnetic characteristics, electrical, and dielectric performance of BTO. By evaluating these high loading levels, this study seeks to identify the solubility threshold and investigate the

resulting functional properties once this limit is exceeded, and optimize the correlation between structure evolution and dielectric behavior. These findings offer new insights into the engineering of dielectric materials through the deliberate exploitation of solubility limits and interphase diffusion, rather than simple lattice substitution, to tailor the dielectric and magnetic response of the resulting composites for advanced energy storage and capacitor applications.

2. Experimental procedure

A series of $BaTiO_3$-(x) wt.% Yb_2O_3 samples ($x = 0$, 2, 5, 10, and 20 wt%) were prepared by conventional solid-state reaction route. Details of the preparation of $BaTiO_3$ (BTO) phase were described elsewhere [33]. In a typical procedure, a proper amount of tetraisopropyl orthotitanate ($Ti[OCH(CH_3)_2$, TTIP, >98%, from ACROS Organics), as a source of titanium, was dissolved in an ethanolic solution under stirring for 30 min at 80 °C. At the same time, a proper amount of barium carbonate ($BaCO_3$, ≥99%, from Sigma Aldrich) was dissolved in another beaker to form a solution of barium citrate. Once obtained, the resultant solution was added to the titanium precursor, and the mixed solution was kept under vigorous stirring and heating. After that, a viscous gel was formed, which was then transferred into an oven for drying and finally calcined at high temperature (600 °C) to form BTO precursor. During the second stage, different amounts of Yb_2O_3 oxide (purity 99%, purchased from Sigma Aldrich) were added to BTO precursor. The powders were weighed according to the desired compositions and mixed in an agate mortar to avoid metallic contamination during the grinding process. Then, the mixture powders were combined with 5 wt% polyvinyl alcohol (PVA) solution as binder, followed by pressing via a hydraulic press to compact them into circular pellets, and finally subjected to sintering temperature at 500 °C for 2 h, followed by 1100 °C for 6 h to obtain compacted $BaTiO_3$-(x) wt.% Yb_2O_3 samples. The samples were coded as BTO, BTO-Yb2, BTO-Yb5, BTO-Yb10, and BTO-Yb20 for BTO added with $x = 0$, 2, 5, 10, and 20 wt% of Yb_2O_3.

The prepared samples were examined via powder X-ray diffraction (Rigaku MiniFlex 600 XRD) technique with Cu-Kα radiation for phases' identification and crystal structural analysis. Match! 4 and FullProf software were used for the identification of phases and Rietveld refinement. Scanning electron microscope (SEM, FEI Quanta FEG) along with energy-dispersive spectroscope (EDX) was used to examine morphology and elemental compositions. The magnetic measurements were performed using a vibrating sample magnetometer (VSM) head coupled to the Quantum Design physical property measurement system (PPMS). The electrical and dielectric properties were measured across a frequency range up to 1 MHz and at temperatures between 20 °C and 120 °C using an Alpha-A high-performance dielectric/impedance analyzer (Novocontrol Technologies).

3. Results and discussions

3.1. Structural analysis

PXRD patterns of BTO/x Yb_2O_3 ceramic samples are given in Fig. 1. The presence of intense and narrow diffraction peaks indicates that all synthesized ceramic samples possess a high degree of crystallinity. The XRD Bragg reflections for the pristine BTO were indexed to a tetragonal perovskite phase, with the *P4mm* space group (reference card 96-150-7757). Fig. 1(b) presents the enlarged XRD patterns of the prepared ceramics in a $2\theta \approx 40$–$48°$. For all samples, a well-resolved doublet of (200)/(002) Bragg reflection was noticed, signifying that the products stabilize within the tetragonal structure. In BTO/x Yb_2O_3 ceramic samples, supplementary peaks

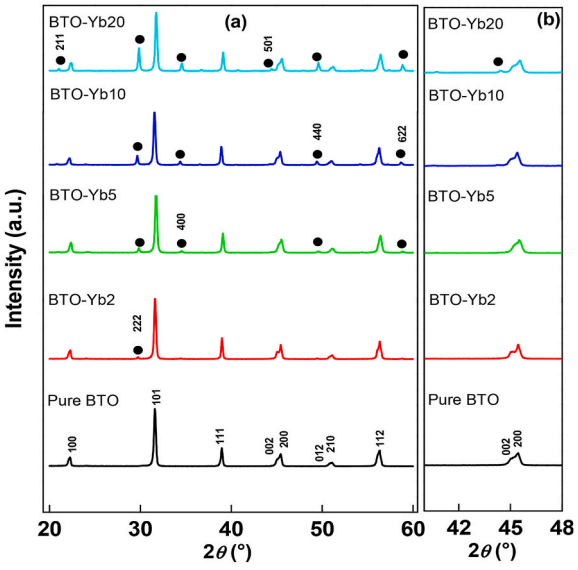

Fig. 1. XRD patterns of BTO, BTO-Yb2, BTO-Yb5, BTO-Yb10, and BTO-Yb20 samples. Dot symbols refer to Yb_2O_3 phase.

related to cubic Yb_2O_3 phase (reference card number 96-153-7840) were detected. Across the entire composition range (2–20 wt%), the presence of XRD diffraction peaks of Yb_2O_3 persist and their intensity increases as increasing their concentrations. This observation indicates that BTO does not remain a single solid-state solution in BTO/Yb_2O_3 ceramic samples, but rather confirms the formation of a composite-like microstructure. The formation of a separate Yb_2O_3 phase indicates that the system exceeds the thermodynamic solubility limit. Previous studies showed the formation of secondary phases in Yb_2O_3-modified BTO, like the pyrochlore-type $Yb_2Ti_2O_7$, due to the lower solid solubility of Yb_2O_3 [34–36].

The cell parameters (*a* and *c*), unit cell volume (*V*), and phase fraction (%) were determined by Rietveld refinement of the experimental XRD data using FullProf and Match! 4 Software (Fig. 2). The different structural parameters extracted from XRD analysis, alongside the R-factors and goodness of fit (χ^2), are listed in Table 1. The χ^2 values ranging from 1.90 to 2.81 demonstrate the high reliability of the structural models. The phase fraction (%) of different phases are too close to the theoretical ones. The *c*/*a* ratio remains higher than 1 for all samples (ranging between 1.0068 and 1.0079), which confirms the persistence of the tetragonal symmetry despite the addition of Yb_2O_3. The unit cell volume "*V*" of the host BTO undergoes a series of contractions and expansions across the entire composition range (2–20 wt%) of Yb_2O_3. This non-linear lattice response indicates that while the majority of Yb_2O_3 additive forms as a separate secondary phase, a specific fraction is successfully incorporating into the BTO lattice and switching sites. This suggests a concentration-dependent site-occupancy transition. The initial contraction may be attributed to some Yb^{3+} ions substituting for A-site (Ba^{2+}), where its significantly smaller radius (~1.01 Å vs. 1.61 Å for 12-fold coordination) leads to a shrinkage of the unit cell. The subsequent fluctuations indicate the amphoteric behavior of the additive, where some of the Yb^{3+} ions (~0.86 Å for 6-fold coordination) may begin to occupy the B-site (Ti^{4+}≈0.60 Å) to minimize lattice strain as the A-site saturates. Other possible reasons for the irregular trend in the unit cell volume likely include the dominance of defect chemistry and vacancy-mediated strain [22]. On the basis of charge neutrality requirements and the ionic radii of the constituents, Ti and Yb are highly expected to maintain their stable oxidation states of 4+ and 3+, respectively. This is supported by the variations in lattice parameters obtained from Rietveld refinement, which align with the substitution of Yb^{3+} into the Ba^{2+} and Ti^{4+} sites.

The crystallite size and lattice strain of BTO/*x* Yb_2O_3 ceramic samples were evaluated using both the Scherrer equation [37] and the Williamson-Hall (W–H) method [38]:

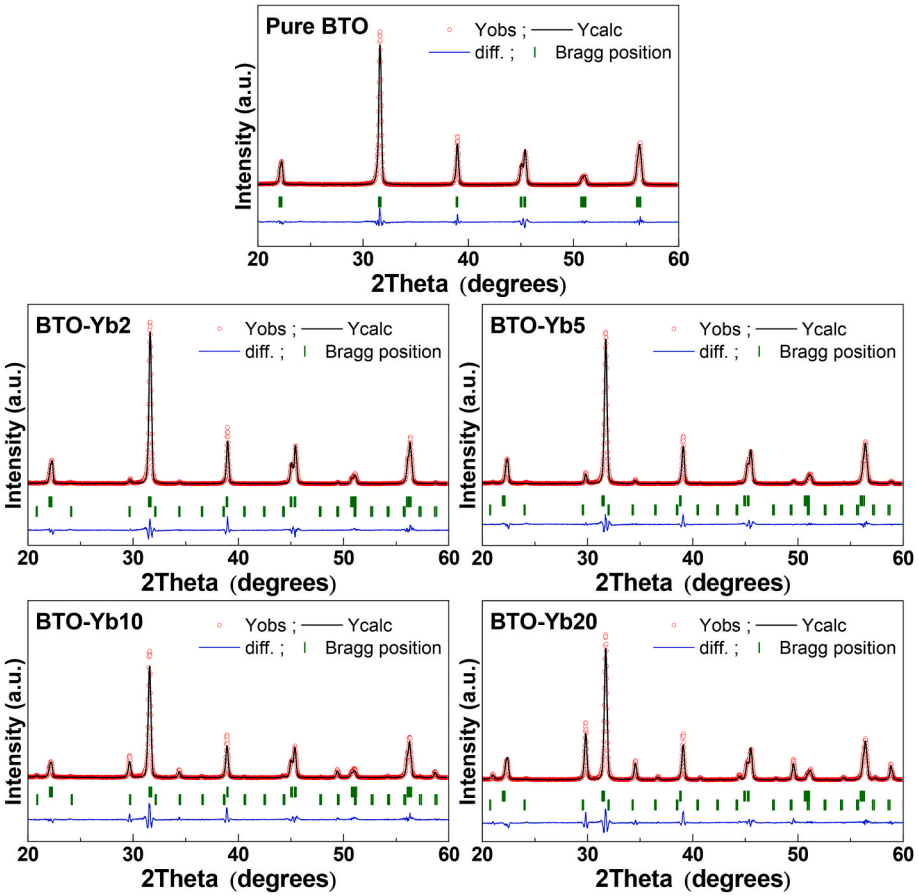

Fig. 2. Rietveld refinement of XRD patterns for BTO, BTO-Yb2, BTO-Yb5, BTO-Yb10, and BTO-Yb20 samples.

Table 1
Refined structural parameters extracted through XRD analysis.

Samples	Phase	Structure	Fraction (%)	a, b (Å)	c (Å)	c/a	V (Å^3)	χ^2	R_{wp}	R_{exp}	R_B	$D_{Scherrer}$ (nm)	$D_{W\text{-}H}$ (nm)	Micro-strain ($\times 10^{-3}$)
Pure BTO	BTO	Tetragonal	100	3.9986 (1)	4.0281 (2)	1.0074	64.406 (4)	2.22	15.9	10.66	3.96	25.84	49.43	2.14
BTO-Yb2	BTO	Tetragonal	97.12	3.9953 (1)	4.0268 (1)	1.0079	64.277 (2)	1.90	16.3	11.82	4.44	30.51	60.85	1.96
	Yb_2O_3	Cubic	2.88	10.4232 (8)		–	1132.42 (14)							
BTO-Yb5	BTO	Tetragonal	95.46	3.9962 (1)	4.0234 (2)	1.0068	64.254 (3)	1.97	16.3	11.63	3.44	30.57	56.57	1.81
	Yb_2O_3	Cubic	4.54	10.4219 (6)		–	1131.99 (12)							
BTO-Yb10	BTO	Tetragonal	91.56	3.9965 (1)	4.0266 (2)	1.0075	64.313 (3)	2.33	18.3	11.98	8.08	31.28	64.65	2.03
	Yb_2O_3	Cubic	8.44	10.4267 (4)		–	1133.56 (7)							
BTO-Yb20	BTO	Tetragonal	80.29	3.9953 (1)	4.0246 (2)	1.0073	64.242 (3)	2.81	17.6	10.50	7.47	30.29	61.10	1.99
	Yb_2O_3	Cubic	19.71	10.4238 (2)		–	1132.61 (4)							

*__Footnote:__ Values in parentheses represent the estimated standard deviations in the last significant digit.

$$D_{Scherrer} = \frac{K\,\lambda}{\beta\,\cos\,\theta} \tag{1}$$

$$\beta\,\cos\,\theta = \frac{K\,\lambda}{D_{W-H}} + 4\varepsilon\,\sin\,\theta \tag{2}$$

in these equations, K, λ, β, θ, and ε represent the shape factor, the X-ray wavelength, the full width at half maximum (FWHM), the Bragg angle, and the micro-strain, respectively. $D_{Scherrer}$ and $D_{W\text{-}H}$ stand for the crystallite size determined by using Scherrer equation and W–H method, respectively. W–H plots ($\beta\,cos\,\theta$ vs. $4\,sin\,\theta$) are presented in Fig. 3. From these plots, the slope gives the micro-strain value, while the y-intercept allows for the calculation of the strain-corrected crystallite size ($D_{W\text{-}H}$). The estimated values are provided in Table 1. As shown, the average crystallite size calculated via the Scherrer formula ($D_{Scherrer}$) ranges from 25.84 nm to 31.28 nm. However, it is well-known that the Scherrer method often results in an underestimation of the grain size as it attributes all peak broadening to crystallite size effects. By employing the W–H method, which deconvolutes size-induced broadening from micro-strain, larger crystallite sizes ($D_{W\text{-}H}$) between 49.43 nm and 64.65 nm were obtained. Interestingly, a simultaneous increase in D and decrease in micro-strain were observed upon the addition of Yb_2O_3 compared to pure BTO sample. This suggests a strain relaxation mechanism facilitated by Yb_2O_3 phase separation. As Yb_2O_3 appears, it may effectively expel excess dopants and lattice defects from the host interior of BTO lattice toward the grain boundaries. This process may lead to a reduction in local strain and promotes grain growth by enhancing atomic diffusion at the grain boundaries. This increased mobility allows the host BTO crystallites to overcome pinning forces and undergo coalescence. These results are consistent with findings by A. Jain et al., who showed a similar increase in crystallite size from 45 nm for pure BSC ceramic to 66 nm for Yb-modified BSC ceramic [36]. Consequently, the consistent increase in crystallite size observed in both models indicates that Yb_2O_3 addition promotes grain growth and aggregation within the BTO matrix.

3.2. Morphological analysis

SEM images of BTO/x Yb_2O_3 ceramics are illustrated in Fig. 4. These ceramics showed a granular structure consisting of

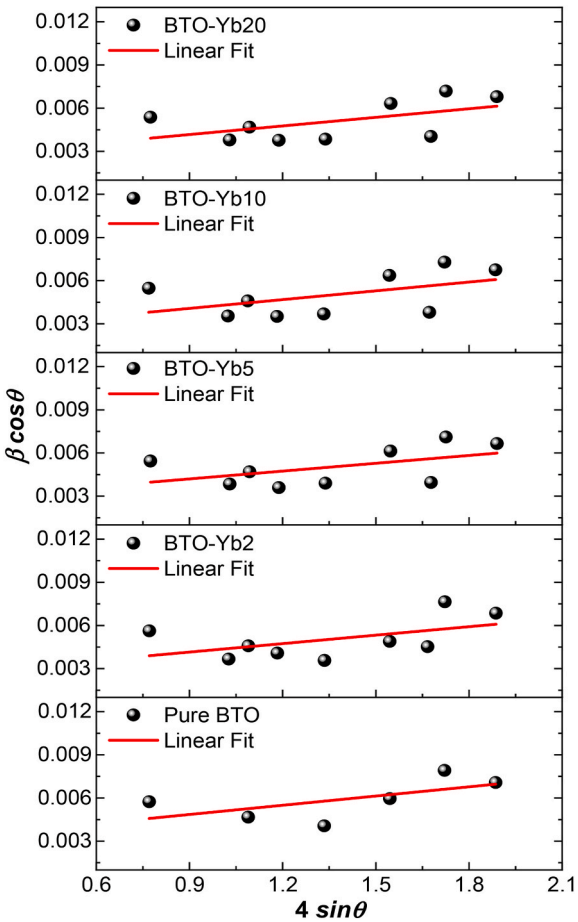

Fig. 3. W–H plots of BTO, BTO-Yb2, BTO-Yb5, BTO-Yb10, and BTO-Yb20 samples.

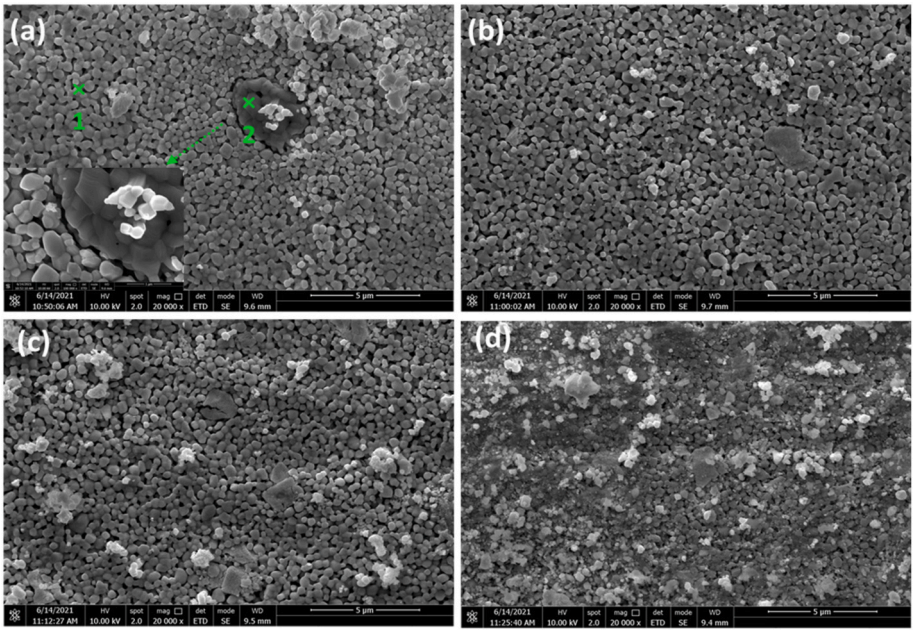

Fig. 4. SEM micrographs of **(a)** BTO-Yb2, **(b)** BTO-Yb5, **(c)** BTO-Yb10, and **(d)** BTO-Yb20 ceramics.

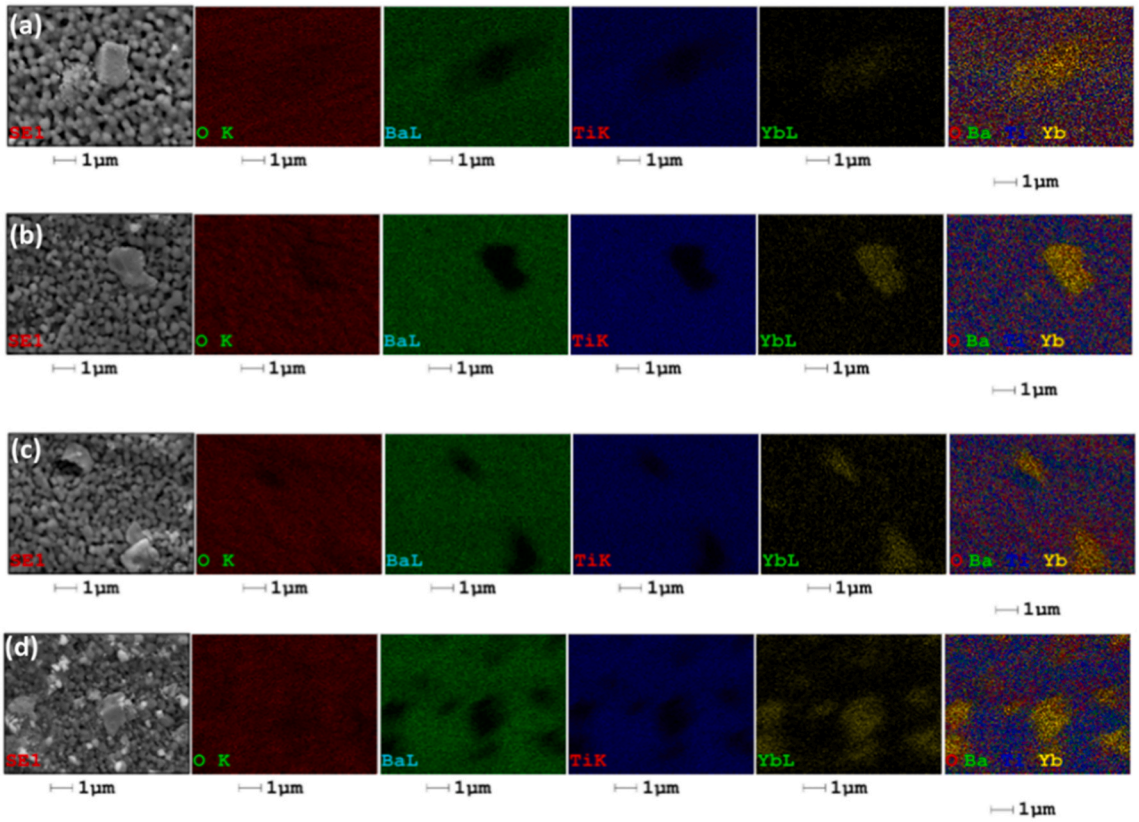

Fig. 5. Elemental mapping of **(a)** BTO-Yb2, **(b)** BTO-Yb5, **(c)** BTO-Yb10, and **(d)** BTO-Yb20 samples showing the distribution of O (red), Ba (green), Ti (blue), and Yb (yellow) overlaid on the secondary electron micrographs.

predominantly quasi-spherical and polyhedral grains' morphology, characteristic of BTO phase. However, a separate phase with a different appearance was also observed, consisting of a lumpy, interspersed granular structure within the BTO granules (Inset Fig. 4 (a)). This secondary structure is indicative of the formation of ceramic-ceramic composites, which agrees with XRD results.

The elemental mapping images for each sample, showing the elemental distribution of Ba, Ti, O, and Yb, were displayed in Fig. 5. The images showed that the elements Ba (green), Ti (blue), and O (red) were distributed consistently on the entire surface of the samples. Whereas the Yb element (yellow) was distributed differently. EDS mapping revealed a somewhat uniform distribution of Yb throughout the grains in BTO-Yb2, suggesting its incorporation into the perovskite lattice. However, as the concentration of Yb_2O_3 increases, a distinct elemental segregation becomes apparent. Yb was mainly concentrated in the regions with a lumpy granular structure. These Yb-rich zones increased with increasing concentrations of Yb_2O_3 in the BTO matrix, resulting in a high density of interfaces between the host and the guest materials. Quantitative analysis on different regions of the samples was performed, and typical EDX spectra and elemental composition are shown in Fig. 6. The spectrum registered on region 1 showed intense signals of Ba and Ti with trivial signals of Yb. However, Yb peaks were prominent in region 2, while the peaks associated with Ba and Ti were very low, confirming its Yb richness.

3.3. Magnetic properties

Fig. 7(a) presents the curves of magnetization versus magnetic field (in the range of ±10 kOe) performed at room temperature for pure BTO, BTO-Yb2, BTO-Yb5, BTO-Yb10, and BTO-Yb20 samples. Generally, in its pure, bulk form, BTO is inherently diamagnetic. Yet, in this study, pure BTO sample shows a slim *M-H* hysteresis loop, establishing its weak room-temperature ferromagnetic behavior. The observed ferromagnetism in BTO sample is primarily intrinsic and native defect-mediated, arising from the existence of oxygen vacancies generated throughout sintering and the associated probable trace reduction of Ti^{4+} ions to Ti^{3+}. Similar observation has been reported by A. Kumar et al. in pure BTO [39]. Upon addition of Yb_2O_3, hysteretic opening near the origin is clearly observed, which indicates that the addition of Yb ions has introduced an ordered magnetic state due to their partially filled 4*f* electron shells, which interact with and amplify the existing defect-driven magnetism of the host BTO lattice. Furthermore, the aliovalent substitution of these Yb^{3+} ions (replacing Ba^{2+} or Ti^{4+}) forces the formation of additional oxygen vacancies to sustain charge neutrality, thereby increasing the density of magnetic polarons. Therefore, the magnetic signature in Yb_2O_3-added samples can be governed by the bound magnetic polaron (BMP) model, where the electrons are trapped within the oxygen vacancies by the intermediate of exchange coupling between Yb^{3+} ions [39,40]. The resulting S-shaped curvature is the classic signature of alignment of magnetic domains and ultimate saturation, where the steep rise near the origin represents the rapid orientation of magnetic moments. However, a downward tilt of the curves at high magnetic fields (the negative slope in the saturated regions) was clearly observed in BTO-Yb2, BTO-Yb5, and BTO-Yb10. This may be ascribed to the intrinsic diamagnetism of the BTO host lattice and the sample holder that provides a larger negative susceptibility than the positive contribution of the Yb magnetic moments [41]. However, this contribution was rigorously subtracted in Fig. 7(b) to isolate the intrinsic magnetic parameters of the material. Notably, a disappearance of the downward diamagnetic tilt was noticed for BTO-Yb20 samples. This signifies a compensation effect, where the strong positive paramagnetic susceptibility of the separate Yb_2O_3 phase cancels out the negative susceptibility of the BTO host. This confirms the formation of composites rather than a simple solid solution. It is noteworthy that the persistence of the ferromagnetic hysteresis loop at the highest loading ratio of 20 wt%, rather than being dominated by paramagnetism, indicates strong interfacial coupling. The oscillatory lattice contraction and expansion observed in XRD and the high density of interfaces between BTO and Yb_2O_3 observed by SEM suggest that the interfaces between the host BTO and the added Yb_2O_3 may act as regions of intense spin-disorder and high vacancy density, stabilizing the ferromagnetic state through a "magnetic proximity effect" [42]. Consequently, the system evolves into a composite where the Yb solubility limit effectively stabilizes the magnetic order, preventing a transition to a purely paramagnetic state even at high Yb_2O_3 concentrations. Fig. 7(b) presents the *M(H)* hysteresis loops of all samples after subtracting the response at high magnetic field. This enables the accurate determination of important magnetic properties, including saturation magnetization (M_s), coercivity (H_c), and remanence (M_r), which are vital for diverse applications. Fig. 8 shows the variations of M_s, M_r, and H_c versus Yb_2O_3 concentration. It is clearly seen that Yb_2O_3 incorporation effectively intensifies the weak ferromagnetism of the host BTO, resulting in a significantly wider (higher coercivity) and

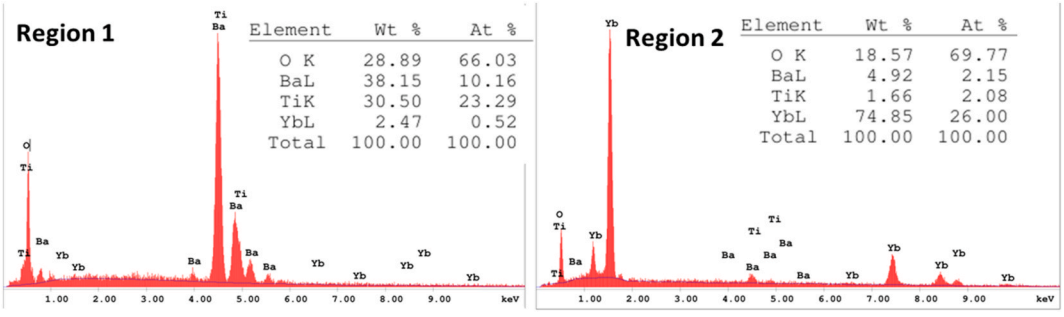

Fig. 6. Typical EDX spectra and elemental composition performed in two different regions of BTO-Yb2 sample. The inset tables summarize the quantitative analysis showing the elemental distribution in weight (wt. %) and atomic (at. %) percentages.

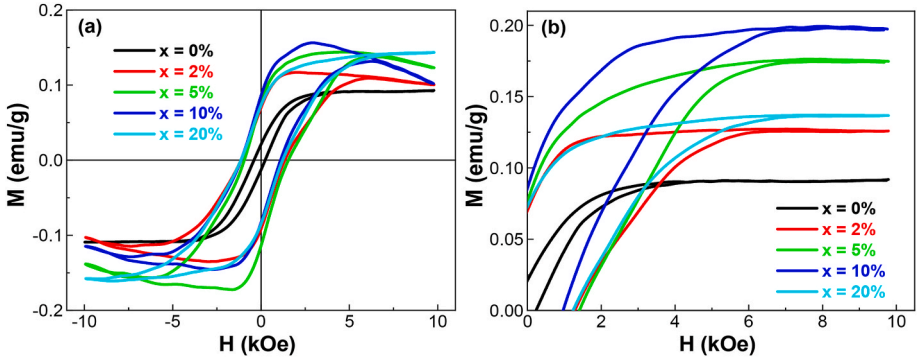

Fig. 7. **(a)** *M(H)* curves for the prepared samples. **(b)** *M(H)* hysteresis loops for the prepared samples after subtraction of the magnetic response at high fields.

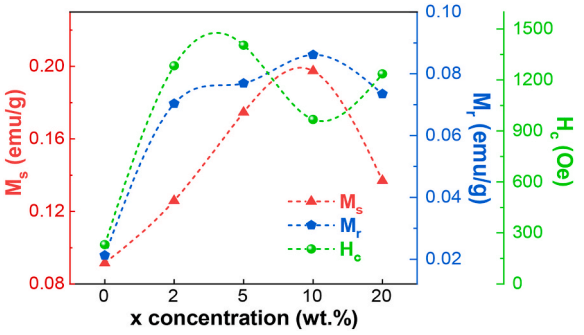

Fig. 8. Variations of M_s (red symbol), H_c (green symbol), and M_r (blue symbols) as a function of Yb_2O_3 concentration. Dashed lines are a guide for the eyes.

taller (higher magnetic saturation) hysteresis loop compared to the pure BTO sample. Remarkably, a decrease in M_s, and M_r coupled with an increase in H_c was noticed at high concentration, which can be ascribed to the increase density of Yb_2O_3 precipitates that reduce the magnetically active ions and disturb long-range magnetic exchange between Yb ions still inside BTO lattice.

3.4. Electrical properties: AC conductivity

To understand conductivity variations, the total conductivity is expressed as [43]:

$$\sigma_{total}(\omega, T, x) = \sigma_{dc}(T, x) + \sigma_{ac}(\omega, T, x) \tag{3}$$

where, $\sigma_{dc}(T,x)$ denotes the direct current (DC) conductivity (independent of frequency), whereas σ_{ac} signifies the alternating current (AC) conductivity (directly linked to the dielectric characteristics of the compound). σ_{ac} is associated with some combined parameters such as the dielectric constant, dielectric loss, and dissipation factor ($tan\ \delta$), and is expressed as [44]:

$$\sigma_{ac} = \omega\varepsilon_0\varepsilon_r(\omega, T, x) tan\ \delta(\omega, T, x) \tag{4}$$

where $\omega(= 2\pi f)$ is the angular frequency, ε_0 is the permittivity of free space, ε_r is the relative dielectric constant, and $tan\ \delta$ is the dissipation factor.

Graphical characterization in Fig. 9 illustrates some changes in σ_{ac} of BTO/x Yb_2O_3 compound within a temperature ranging from 20 °C to 120 °C. An enlargement in σ_{ac} with increasing frequency has been noticed across all compounds. This occurrence can be elucidated by the transfer of charge carriers between localized states. Therefore, the externally applied electric field (frequency) acts as a driving force that facilitates the release of the trapped charges. For pure BTO, σ_{ac} reveals a low-frequency distribution followed by a power-law increase at higher frequencies [45]. This kind of trend suggests hopping conduction of charge carriers where conductivity is affected by thermally activated polaron jumps [46]. As in the examples of BTO-Yb2, BTO-Yb5, BTO-Yb10 and BTO-Yb20, the overall conductivity is lower and the frequency dependence becomes less pronounced; this likely indicates a reduction in carrier mobility due to potential defect trapping [47]. In pure Yb_2O_3, σ_{ac} is significantly lower at low frequencies but rises sharply at high frequencies; this suggests a possible transition to a more insulating phase via hopping conduction between localized carriers and defect states [48,49]. That is, the temperature-dependent behavior follows Arrhenius-type behavior and further confirms the role of oxygen vacancies and defect states in conduction mechanisms [50]. Intrinsic conduction in pure BTO is primarily governed by oxygen vacancies, which act as

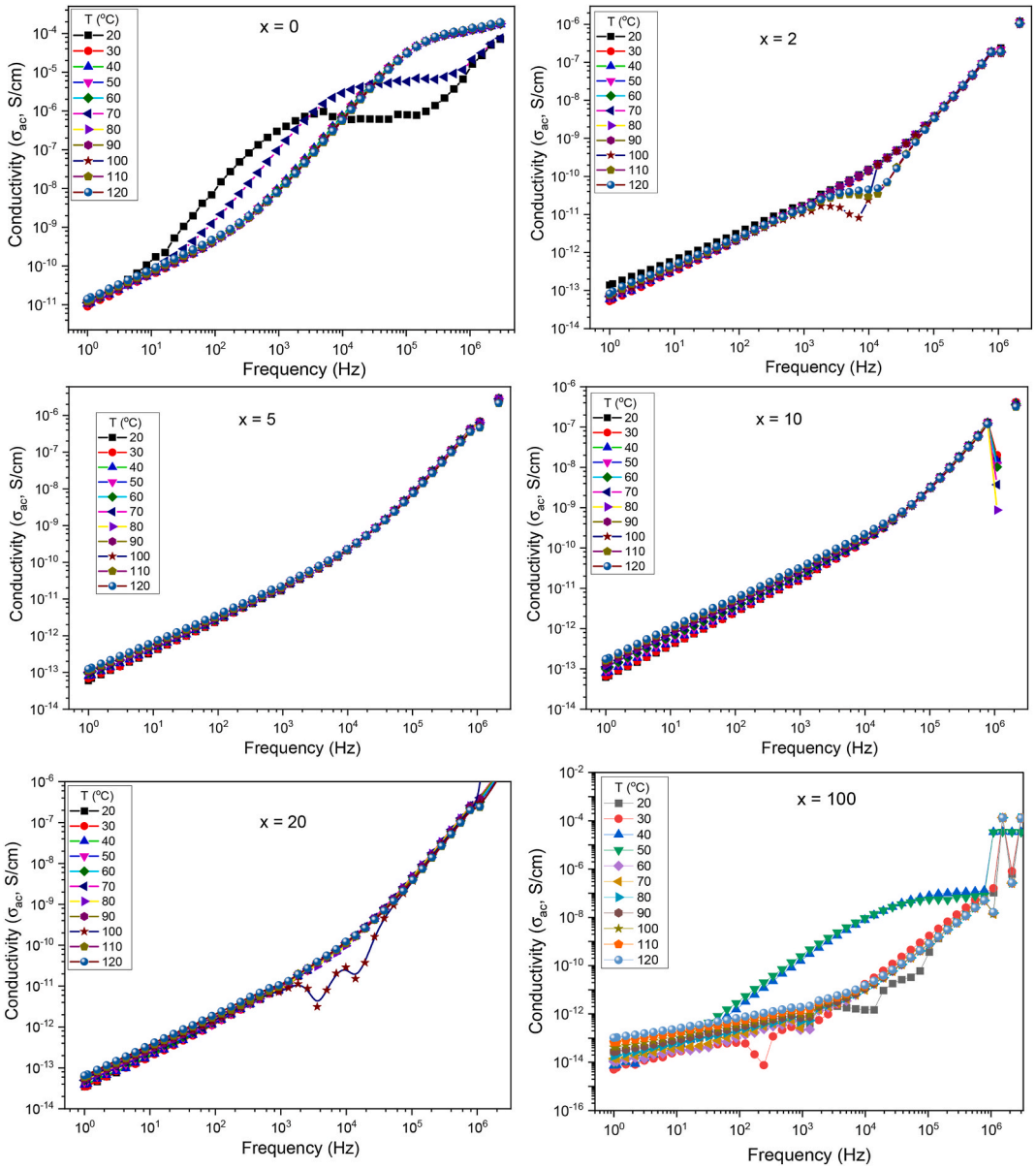

Fig. 9. *ac* conductivity of pure BTO, BTO-Yb2, BTO-Yb5, BTO-Yb10, BTO-Yb20, and pure Yb_2O_3 samples. *As control, data of x = 0% samples were reused with permission from* Ref. [45].

electron donors at high temperatures [51]. Moderate addition of Yb_2O_3 (x = 2-10 wt%) may introduce localized defect states that require additional activation energy for carrier excitation, leading to reduced conductivity [29]. In moderately added samples, enhanced grain boundary conduction is likely responsible for the observed trends, as previously reported for rare-earth-modified titanates [52].

The AC conductivity of the BTO/Yb_2O_3 samples displays a complex dependence on the concentration of additive. The significant increase in conductivity at higher frequencies confirms the occurrence of polaron hopping in the BTO structure. However, in BTO added with Yb_2O_3, the effective capture of charge carriers by Yb ions results in a reduction of charge carriers participating in short-range intra-well hopping, leading to a slight decrease in overall conductivity. This decline is mostly ascribed to the effective capture of charge carriers by Yb^{3+} ions and the occurrence of resistive secondary phases at the grain boundaries, which would diminish the number of carriers that can participate in the short-range intra-well hopping. Moreover, variations in particle size at higher concentrations may enhance scattering mechanisms, which further impede charge transport. In conclusion, the observed trends in σ_{AC} indicate a strong dependence on Yb_2O_3 concentration, with moderate Yb_2O_3 addition can be used to optimize charge transport, while excessive concentrations of additives lead to significant defect-induced carrier trapping. These findings highlight the tunability of BTO-based materials for specific electronic and dielectric applications.

To further understand the conduction mechanism, the frequency dependence of σ_{AC} was quantitatively investigated using *UJPL*, which is commonly used to describe charge transport in disordered dielectric materials. The relationship between conductivity and frequency can be expressed as follows:

$$\sigma_{ac}(f) = \sigma_{dc} + Af^{s} \tag{5}$$

where σ_{dc} denotes the frequency-independent DC conductivity, A represents a temperature-dependent constant, f is the frequency, and s stands for the frequency exponent that reflects the dominant charge transport mechanism. As observed in Fig. 10, it is evident that the $\sigma_{ac}(f)$ spectra of $BaTiO_3/xYb_2O_3$ ceramics exhibit a characteristic dispersion behavior comprising a low-frequency plateau followed by a gradual improvement in conductivity at higher frequencies. Therefore, this behavior is characteristic for many oxide ceramics and ultimately demonstrates that charge transport occurs via a hopping process between localized states.

The measured conductivity spectra were fitted using JPL, and the extracted parameters (i.e., σ_{dc}, A and s) are outlined in Table 2. The frequency exponent s was found to lie in the range of approximately 0–1 for all compositions and temperatures, confirming that the AC conduction arises from a hopping mechanism of localized charge carriers. Furthermore, the temperature dependence of s exhibits a gradual decline with elevating temperature. Such trend is collectively associated with the correlated barrier hopping (CBH) model, in which charge carriers hop among defect states isolated by potential barriers that are lowered with growing thermal energy. Therefore, the measured conductivity dispersion in $BaTiO_3/Yb_2O_3$ ceramics can be assigned to thermally-activated hopping of localized charge carriers, most likely associated with defect states and oxygen vacancies within the ceramic matrix. These consequences provide

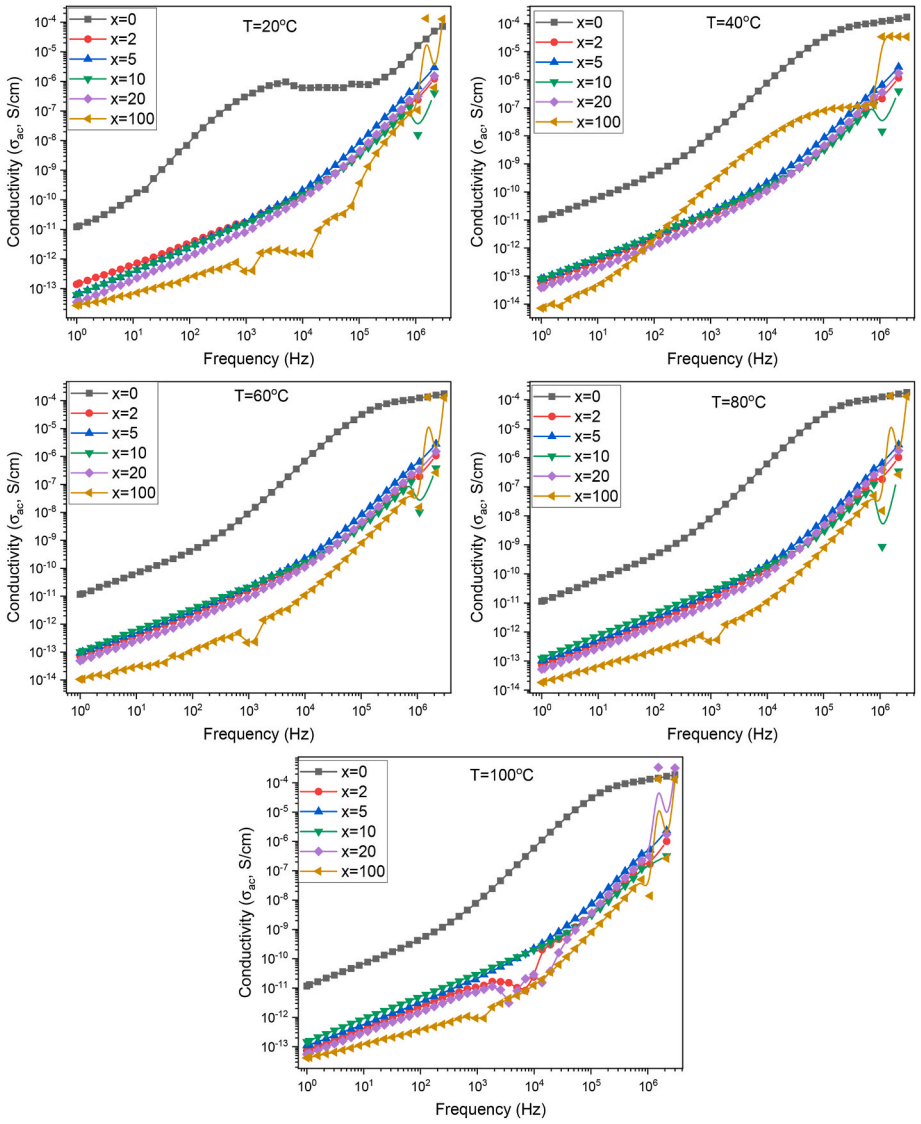

Fig. 10. AC conductivity of $BaTiO_3/xYb_2O_3$ ceramics with x = 0, 2, 5, 10, 20 and 100%.

Table 2
JPL fitting parameters for $BaTiO_3/xYb_2O_3$ ceramics.

Sample	T (°C)	σ_{dc} (S/cm)	A (S·s^s)	s
Pure BTO	**20**	2.1×10^{-12}	4.5×10^{-15}	0.82
	60	7.6×10^{-12}	1.3×10^{-14}	0.78
	100	2.9×10^{-11}	3.8×10^{-14}	0.73
BTO-Yb2	**20**	1.6×10^{-12}	3.1×10^{-15}	0.84
	60	6.2×10^{-12}	9.7×10^{-15}	0.80
BTO-Yb5	**20**	9.4×10^{-13}	2.2×10^{-15}	0.86
BTO-Yb10	**20**	5.1×10^{-13}	1.4×10^{-15}	0.88
BTO-Yb20	**20**	2.7×10^{-13}	8.5×10^{-16}	0.89

measurable support for the proposed polaron-assisted conduction mechanism in the examined ceramics.

It is well known that the conduction mechanism in the characterized BTO/Yb_2O_3 ceramics can be explained easily by thermally activated hopping of localized charge carriers. Thus, σ_{AC} spectra are observed to exhibit a typical frequency dispersion feature of hopping conduction in disordered oxide ceramics. At lower temperatures and frequencies, charge transport is primarily manipulated by localized carriers associated with oxygen vacancies and defect states. As the frequency elevates, the conduction mechanism transforms into short-range hopping of charge carriers between localized states. The low E_A's (10–130 meV) extracted from Arrhenius plot analysis indicate that conduction is primarily dominated by small polaron hopping and defect-mediated electron transport associated with oxygen vacancies and Ti^{3+} ion centers formed during sintering. Additionally, the occurrence of Yb_2O_3 secondary phases further contributes to grain-boundary controlled conduction by forming high-resistance grain boundaries.

3.5. *Electrical properties: DC electrical conductivity and activation energy*

DC electrical conductivity (σ_{dc}) and activation energy (E_a) of pure BTO, pure Yb_2O_3, BTO-Yb2, BTO-Yb5, BTO-Yb10, and BTO-Yb20 samples are presented in Fig. 11. The addition of Yb_2O_3 in varying concentrations effectively tunes both σ_{dc} and E_a. The relationship between σ_{dc} and temperature follows the Arrhenius equation:

$$\sigma_{dc}(T,x) = \sigma_0(x) exp\left(-\frac{E_a(T,x)}{k_B T}\right) \tag{6}$$

where $\sigma_{dc}(T,x)$ denotes the DC conductivity at a given temperature T and dopant concentration x, $\sigma_0(x)$ stands for the pre-exponential factor dependent on doping concentration, $E_a(T,x)$ signifies the activation energy, which alters with both temperature and dopant concentration, and k_B being the Boltzmann constant.

Arrhenius plot of σ_{dc} versus the reciprocal temperature ($1000/T$) is depicted in Fig. 11 (left) for BTO, pure Yb_2O_3, BTO-Yb2, BTO-Yb5, BTO-Yb10, and BTO-Yb20 samples, illustrating that σ_{dc} increases with temperature, which determines the thermally activated transport of charge carriers. The slope of each curve in the Arrhenius plot directly is related to the E_a for charge transport. Typically, abrupt slopes suggest higher energy barriers for charge carriers, as reported in earlier findings on modified BTO [65]. The incorporation of Yb_2O_3 conducts to substantial changes in σ_{dc}, mainly because of variations in charge carrier density and mobility. The relationship between activation energy (E_a) and Yb_2O_3 levels provides further comprehension into charge transport mechanisms, as shown in Fig. 11 (right): firstly, pure $BaTiO_3$ ($x = 0\%$) exhibits the lowest E_a (~10 meV), suggesting intrinsic conduction dominated by oxygen vacancies [66]. Secondly, for moderate x levels (BTO-Yb2 and BTO-Yb5 samples), E_a initially increases, indicating the formation of shallow defect states that require supplementary energy for carrier excitation [67]. Thirdly, beyond $x = 5$ wt%, a reduction in E_a suggests improved charge transport owing to enhanced grain boundary conduction, akin to findings in other RE-modified titanates [68]. Lastly, a sharp hopping process in E_a from ~30 meV to ~130 meV for pure Yb_2O_3 ($x = 100\%$) indicates a transition to an insulating phase, ascribed to charge carrier localization and reworked band structure [69]. Higher x contents give rise to meaningfully

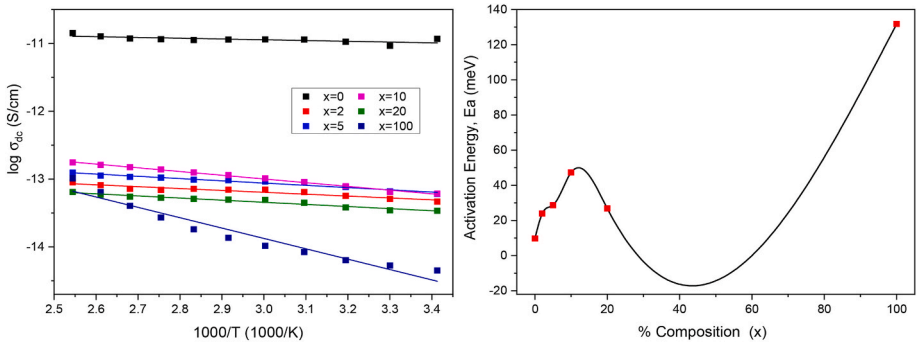

Fig. 11. dc conductivity **(Left)** and activation energy **(Right)** of pure BTO, pure Yb_2O_3, BTO-Yb2, BTO-Yb5, BTO-Yb10, and BTO-Yb20 samples.

lower conductivity, which can be attributed to defect formation and charge carrier trapping at grain boundaries [26]. Moderate Yb_2O_3 content ($x = 2$–10 wt%) enhances σ_{dc} by optimizing charge carrier density and mobility, making BTO a viable candidate for electronic applications like capacitors and resistors. By understanding the interaction between substituent/dopant concentration, conductivity, and E_a, this study highlights the potential of Yb_2O_3-modified BTO for customized material design in advanced technological applications.

3.6. Complex permittivity: dielectric constant

The dielectric characteristics of BTO/$x$$Yb_2O_3$ are governed by various polarization mechanisms, including dipolar, electronic, atomic, and space charge polarization. In the presence of a time-varying electric field, the dielectric constant assumes a complex nature, mathematically expressed as [70]:

$$\varepsilon^*(\omega, T, x) = \varepsilon_r(\omega, T, x) + j\varepsilon_i(\omega, T, x) \tag{7}$$

where $\varepsilon_r(\omega, T, x)$ and $\varepsilon_i(\omega, T, x)$ represent the real and imaginary components, respectively. These components describe the stored and dissipated energy within the material, both of which depend on frequency, temperature, and dopant concentration. The real part, ε_r, can be determined using the relation [43,71]:

$$\varepsilon_r(\omega, T.x) = \frac{C_p(\omega, T, x)t}{\varepsilon_o A} \tag{8}$$

where the parameters retain their conventional meanings. The imaginary part ε_i, is calculated as:

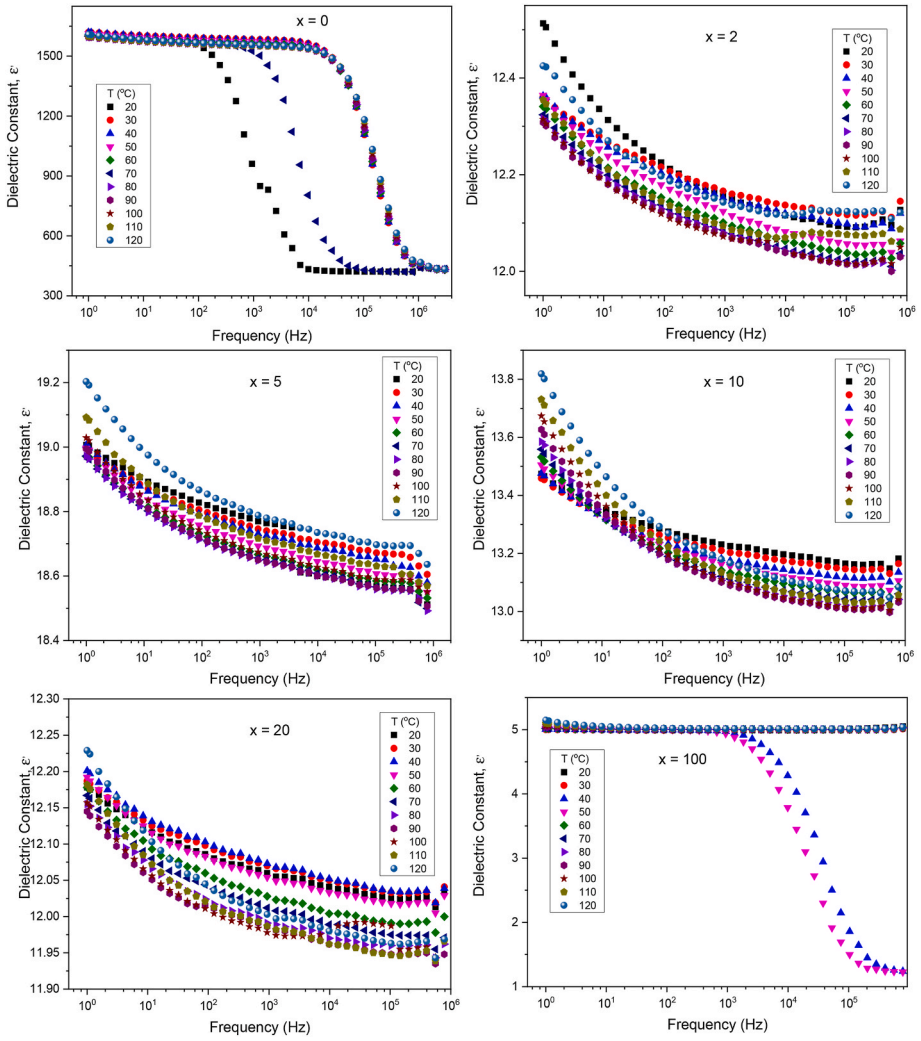

Fig. 12. Dielectric constant of BTO/$x$$Yb_2O_3$ samples. *As control, data of $x = 0\%$ samples were reused with permission from* Ref. [45].

$$\varepsilon_i(\omega,t,x)=\varepsilon_r(\omega,T,x)tan\,\delta(\omega,T,x) \quad (9)$$

The frequency-dependent dielectric constant (ε_r) and loss (ε_i) across a temperature range of 20 °C to 120 °C for different BTO/xYb$_2$O$_3$ samples are graphically illustrated in Figs. 12 and 13, respectively. For pure BTO, the dielectric constant displays a clear dependence on both temperature and frequency. At low frequencies, it exceeds 1500, whereas at high frequencies, it sharply declines to approximately 350 [45]. In contrast, BTO-Yb2, BTO-Yb5, BTO-Yb10, and BTO-Yb20 samples exhibit considerably lower dielectric constant values, ranging between 5 and 20. This substantial decline of ε_r in the modified BTO/Yb$_2$O$_3$ samples compared to pure BTO could be ascribed to the transformation from a single-phase ferroelectric system to a composite-like microstructure system. As the concentration of Yb$_2$O$_3$ (2–20 wt%) looks like exceeding the solubility limit, the high-permittivity BTO matrix is progressively diluted by the separate and low-permittivity cubic Yb$_2$O$_3$ phase (which exhibits $\varepsilon_r \sim 5$). Moreover, the amphoteric nature of Yb^{3+} ions pushes their distribution among A and B sublattices, which very likely interrupts the long-range dipolar coupling required for the high ε_r of the tetragonal BTO lattice. This interruption, along with the creation of resistive Yb-rich secondary phases at the grain boundaries, locks the polarization mechanisms and moves the dielectric response to the low values trait of the insulating Yb$_2$O$_3$ additive.

Overall, ε_r of different samples declines with the increase in frequency. At low frequency regions, the higher values could be ascribed to space charges' polarization derived from the accumulation of charges at grain boundaries and interfaces between the sample and electrodes. However, as frequency increases, space charge polarization becomes less significant, allowing electronic and atomic polarization mechanisms to dominate. At higher frequencies, the dielectric constant stabilizes because dipoles can no longer follow the field, leading to a stable high-frequency dielectric constant [43,71]. For different added BaTiO$_3$ samples (i.e., BTO-Yb2, BTO-Yb5, BTO-Yb10, and BTO-Yb20) at low frequencies, a slight increase in ε_r with increasing Yb$_2$O$_3$ additive is observed compared to the base modified values. This behavior can be attributed to the role of Yb ions in interfacial charge transfer. This

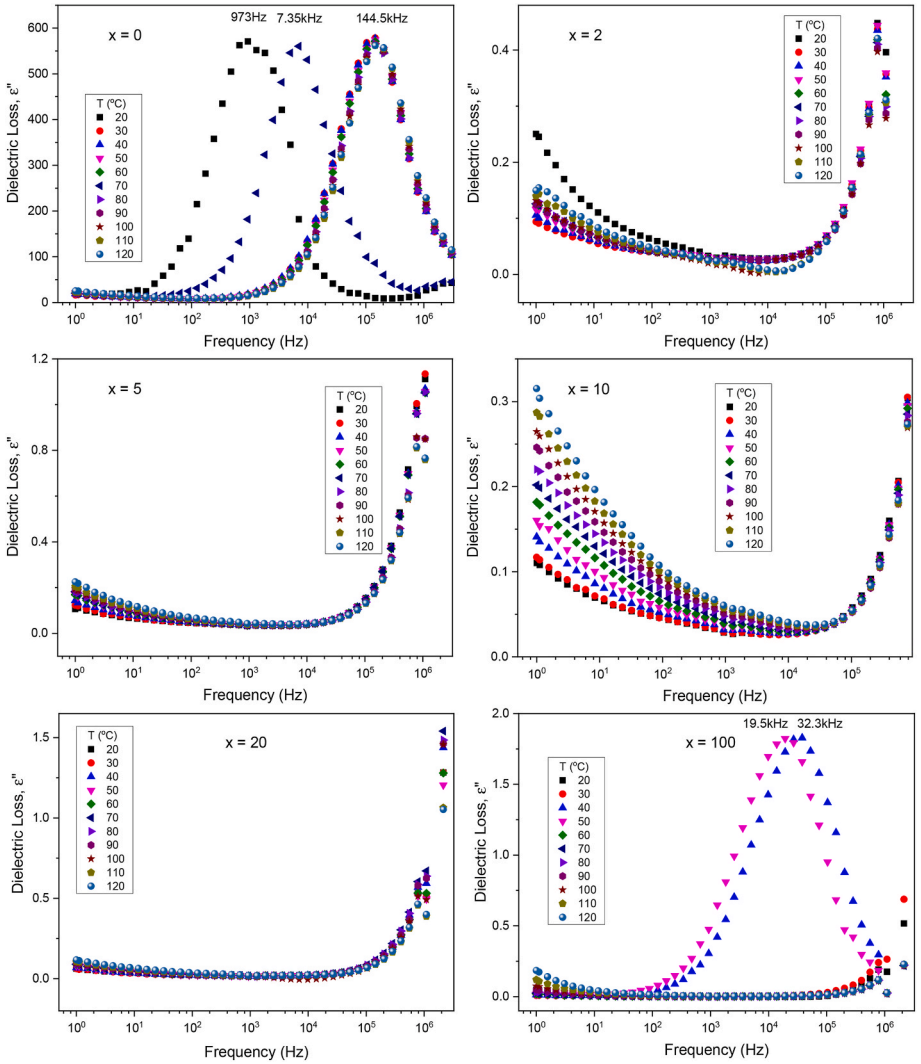

Fig. 13. Dielectric loss of BTO/xYb$_2$O$_3$ samples. *As control, data of x = 0% samples were reused with permission from* Ref. [45].

dielectric dispersion (which diminishes with rising frequency and turns out to be practically constant at high frequency regions) and the temperature-dependent dielectric properties can be further analyzed using the Maxwell-Wagner bilayer model. This model emphasizes the influence of dipolar and interfacial polarization mechanisms [26,72,73]. Although BTO/$x$$Yb_2O_3$ samples follow nearly similar frequency and temperature trends, pure Yb_2O_3 (x = 100%) demonstrates a nearly frequency-independent ε_r, maintaining a stable value of ~5. However, at 40 and 50 °C, a sudden drop from 5 to 1 is observed, resembling the behavior of pure $BaTiO_3$.

It is clear that RE element substitution/doping or RE_2O_3 addition is widely used to modify the dielectric properties of $BaTiO_3$ ceramics (Table 3). Reported ε_r's for RE-modified $BaTiO_3$ systems typically range from ~600 to ~13,000, depending on substituent/additive type, concentration, grain size, and defect chemistry. In many cases, RE ions act as donor substituents when substituting at the Ba^{2+} site, refining polarization and dielectric constant. However, smaller RE ions such as Yb^{3+} tend to occupy the Ti^{4+} site or isolate at grain boundaries, modifying meaningly charge compensation and polarization mechanisms. In contrast to these dielectric mechanisms, the current $BaTiO_3$/Yb_2O_3 ceramics expose much lower dielectric constants (~5–20). This lessening is ascribed to the formation of a composite-like microstructure, in which the low-constant Yb_2O_3 secondary phase dilutes the high-constant $BaTiO_3$ matrix and withholds long-range ferroelectric polarization. The extraordinary decrease in dielectric constant from ~1500 in pure $BaTiO_3$ to ~5–20 in the Yb_2O_3-modified BTO samples can be predominantly attributed to the composite nature of the system rather than intrinsic lattice substitution effects. XRD and SEM analyses clearly show that Yb_2O_3 forms as a separate secondary phase due to the limited solubility of Yb^{3+} ions in the $BaTiO_3$ lattice. Subsequently, the dielectric response is dominated by extrinsic composite effects resulting from the dilution of the high-permittivity $BaTiO_3$ matrix by the low-permittivity Yb_2O_3 phase. Therefore, the dielectric behavior of the present system results from two combined effects which is initially limited intrinsic substitution of Yb^{3+} in the BTO lattice and secondly being dominant extrinsic composite effects caused by phase segregation.

3.7. Complex permittivity: dielectric loss

The dielectric loss of BTO/$x$$Yb_2O_3$ (x = 0, 2, 5, 10, 20, and 100%) exhibits distinct variations across different temperatures and frequencies, as illustrated in Fig. 13. For pure BTO sample, the dielectric loss presents three prominent peaks centered at 973 Hz, 7.35 kHz, and 144.5 kHz, each reaching values around 600. However, for BTO-Yb2, BTO-Yb5, BTO-Yb10, and BTO-Yb20 samples, the dielectric loss is significantly reduced, remaining below 0.4. In general, in all compositions, the dielectric loss decreases with increasing frequency up to a certain point, after which it begins to rise again. The observed dielectric loss behavior follows an exponential relationship with the applied frequency, similar to the dielectric constant. This exponential dependence manifests itself in two different frequency regimes: low and high frequencies. While BTO-Yb2, BTO-Yb5, BTO-Yb10, and BTO-Yb20 exhibit similar frequency and temperature dependence trends, pure Yb_2O_3 (x = 100%) was observed to behave differently. Specifically, the dielectric loss remains almost frequency-independent and stays at a constant value of less than 0.2, except for the appearance of two peaks at 19.5 kHz and 32.3 kHz at 40 °C and 50 °C, respectively; this is noteworthy as it is similar to the behavior observed in pure BTO. Furthermore, the temperature dependence is most pronounced in the BTO-Yb10 sample, thus demonstrating the highest sensitivity to thermal changes. It is important to emphasize that the loss spectra of both pure and BTO/$x$$Yb_2O_3$ samples reveal peaks at certain characteristic frequencies, indicating the presence of relaxing dipoles with varying relaxation strength and frequency depending on relaxation mechanisms.

Dielectric loss arises from energy dissipation due to various mechanisms including resonance and molecular rotations originating from domain walls, ionic conduction, and electronic polarization. In these compositions, polarization affects rotational motion and inhibits domain wall motion at higher frequencies, consequently leading to a reduction in dielectric loss. In particular, dielectric loss becomes significantly important when defects cause polarization to lag behind the applied field [31,74]. It is evident that a slight increase in dielectric loss is observed among the modified samples as the Yb_2O_3 concentration in the composition increases; this increase may indicate changes in the energy dissipation mechanisms and charge carrier dynamics within the material [30,72,73].

3.8. Complex permittivity: dissipation factors

The dissipation factor (tangent loss, tanδ) of BTO/$x$$Yb_2O_3$ (x = 0, 2, 5, 10, 20, and 100%) exhibits distinctive variations across various temperatures and frequencies, as illustrated in Fig. 14. For pure BTO, tanδ exhibits three prominent peaks centered at 2.9 kHz, 14.6 kHz, and 335.0 kHz, each reaching values around 0.7. However, in the BTO-Yb2, BTO-Yb5, BTO-Yb10, and BTO-Yb20 samples, tanδ decreases significantly and remains below 0.02. In general, in all compositions, tanδ decreases with increasing frequency up to a certain threshold, beyond which it begins to rise again. At low frequencies, all ceramics, therefore, disclose a significant temperature and frequency dependence, with peak values occurring at higher temperatures in the low-frequency region. In particular, temperature dependency is most pronounced in the BTO-Yb10 sample only, which indicates the highest sensitivity to thermal changes. While BTO-Yb2, BTO-Yb5, BTO-Yb10, and BTO-Yb20 samples exhibit similar trends in frequency and temperature dependence, the pure Yb_2O_3 sample behaves differently, particularly showing that the loss factor remains almost independent of frequency, and it is possible for it to stay at a constant value lower than 0.01, except for two peaks of approximately 0.75 at 53.5 kHz and 101.4 kHz at 40 °C and 50 °C. The studied tanδ trends may be due to the Shockley-Read process, where the electron capture process increases with temperature, thus strengthening its tanδ value. In addition, the increase in dielectric loss at high temperatures is mainly attributed to the polarization of space charges [75]. This occurs on the surface of the material when defect or impurity ions capture free charge carriers and lead to increased energy dissipation. In particular, precise manipulation of the dissipation factor is critical to optimizing these materials when a balance is to be achieved between dielectric losses and energy storage efficiency. Consequently, the dissipation factor of BTO/$x$$Yb_2O_3$ provides valuable information about dielectric loss and serves as a key parameter to improve the performance in various technological

Table 3
Dielectric constant of some RE-modified $BaTiO_3$ reported in the literature for comparison.

RE ion	Composition	Frequency	Dielectric constant (ε_r)	Main observation	Ref.
La^{3+}	$Ba_{1-X}La_XTiO_3$	1 kHz	250–450	Donor doping enhances dielectric response and shifts Curie temperature	[53]
Nd^{3+}	Nd-doped $BaTiO_3$	1 kHz	1500–3000	Defect dipoles enhance dielectric polarization	[54,55]
Sm^{3+}	Sm-doped $BaTiO_3$	1 kHz	1000–13000	High permittivity due to domain wall mobility and donor substitution.	[56]
Dy^{3+}	Dy-doped $BaTiO_3$	1 kHz	1000-5600	Diffuse phase transition & improved dielectric features	[57]
Ho^{3+}	Ho-doped $BaTiO_3$	1 kHz	300–2000	Enhanced dielectric stability for MLCC applications	[58]
Er^{3+}	Er-doped $BaTiO_3$	1 kHz	2500 – 4500	Grain boundary stabilizing reduces loss.	[59]
Y^{3+}	$BaTiO_3$–Y_2O_3	1 kHz	800–1600	Amphoteric substitution affects dielectric response	[9,60]
Gd^{3+}	Gd-doped $BaTiO_3$	1 kHz	1000–2500	Improved dielectric stability and grain boundary influences	[61]
Ce^{3+}	Ce-doped $BaTiO_3$	1 kHz	900–1700	Donor substitution enhances permittivity and decreases loss	[62,63]
Yb^{3+} (low)	$BaTiO_3$–Yb_2O_3	1 kHz	600–1400	Limited liquid solubility and defect-controlled polarization	[49,64]
This work	Yb_2O_3-modified $BaTiO_3$ (2–20 wt%)	up to 1 MHz	5–20	Composite microstructure with Yb_2O_3 secondary phase reduces dielectric constant	Present study

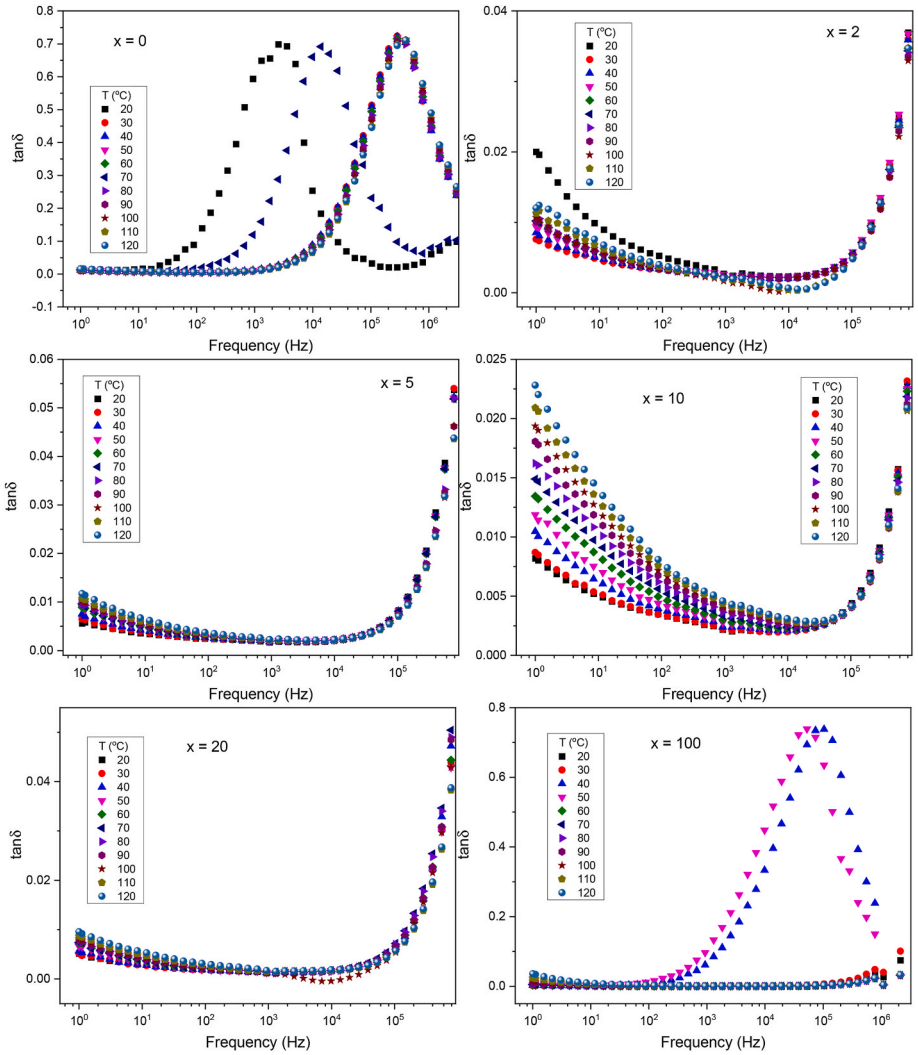

Fig. 14. Dissipation factor of BTO/xYb$_2$O$_3$ ceramics. *As control, data of x = 0% samples were reused with permission from* Ref. [45].

applications.

3.9. Cole-Cole complex impedance analysis

Cole-Cole analysis of complex impedance provides better understandings into charge transport mechanisms, relaxation processes, and interfacial polarization effects within the material. The complex impedance (Z^*) is expressed as [70]:

$$Z^* = R_{ct} + (j\omega C_{dl})^{-1} \tag{10}$$

where R_{ct} stands for the charge transfer resistance and C_{dl} represents the double-layer capacitance. The Nyquist plots presented in Fig. 15 illustrate the imaginary impedance ($-\mathrm{Im}Z_s$) versus real impedance ($\mathrm{Re}Z_s$) through various temperatures for the samples of BTO/xYb$_2$O$_3$ (x = 0, 2, 5, 10, 20, and 100%).

In the pure BTO sample, an increase in temperature typically leads to an increase in $-\mathrm{Im}Z_s$, exhibiting enhanced polarization and capacitive behavior. Simultaneously, $\mathrm{Re}Z_s$ decreases with increasing temperature, indicating an improvement in conductivity. While conventional Nyquist diagrams are typically semi-circular, the present graph shows a known sloping/curved linear trend. As is known, this slope reflects the dominant capacitive effects and high resistance. At low frequencies, the $\mathrm{Re}Z_s$ values remain relatively high, reflecting the insulating nature of the material. Conversely, in the high-frequency regions, $\mathrm{Re}Z_s$ decreases, implying the activation of a conduction mechanism. A detailed inset within the graph reveals a change in slope along with the presence of a small loop in the low-frequency regions. This behavior is an expected outcome suggesting the involvement of multiple charge-transport mechanisms, such as grain boundary and surface effects.

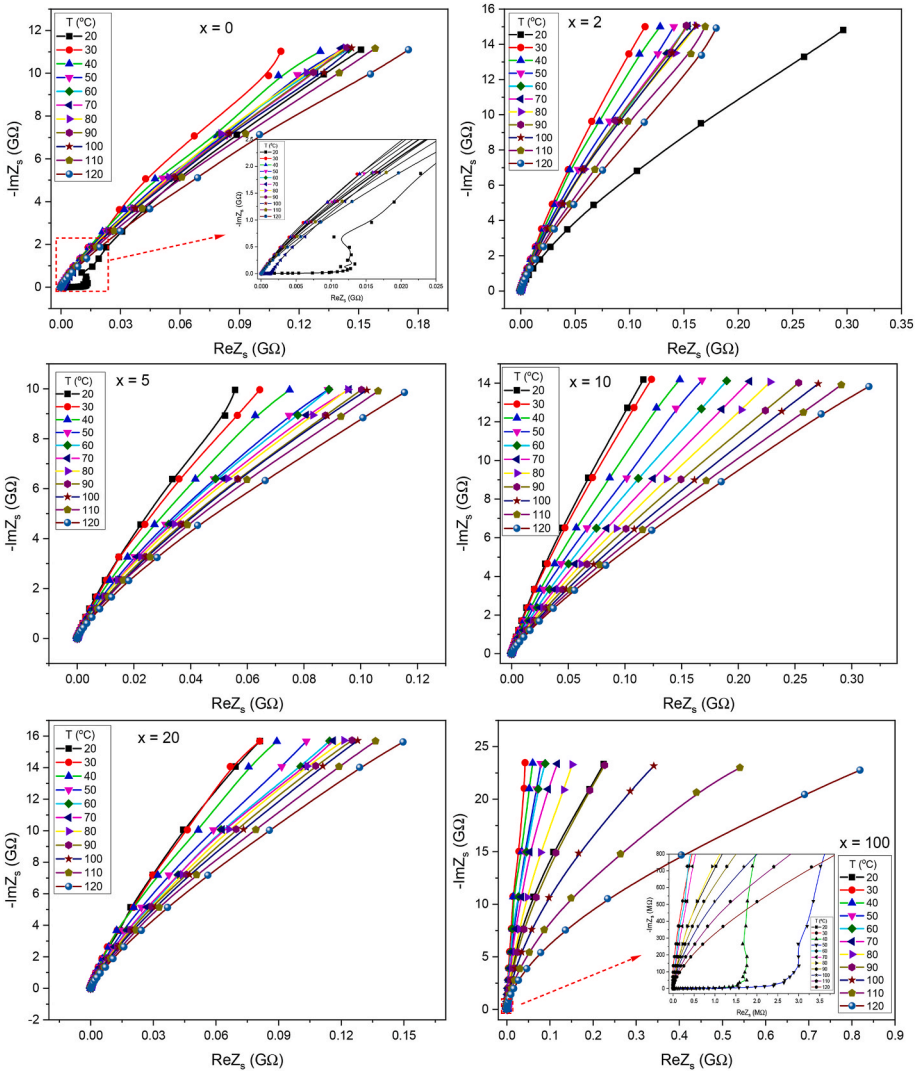

Fig. 15. Nyquist plotting of BTO/xYb$_2$O$_3$ ceramics. *As control, data of x = 0% samples were reused with permission from* Ref. [45].

The BTO-Yb2, BTO-Yb5, BTO-Yb10, and BTO-Yb20 samples exhibit a similar trend. Instead of the traditional semicircular arcs, these data show an almost linear increase, indicating high resistivity and capacitive behavior. As the temperature elevates from 20 °C to 120 °C, the peak of the curves shifts upwards, showing stronger capacitive interactions. The noticed dispersion, with ReZ$_s$ remaining high at low frequencies (right region) and decreasing at high frequencies (left region), highlights the dominance of capacitive contribution and suggests that the incorporation of Yb$_2$O$_3$ alters the conduction mechanism. Similarly, for the pure Yb$_2$O$_3$ sample, the increase in temperature causes an increase in −ImZ$_s$, indicating more pronounced capacitive contribution at higher temperatures. Simultaneously, ReZ$_s$ displays a significant decrease with increasing temperature, suggesting increased conductivity. As with other modified compositions, the absence of a semicircular arc favoring a sloping line between −ImZ$_s$ and ReZ$_s$ confirms its dominant capacitive behaviours and internal resistivity. The supplementary region at lower frequencies again reveals a small slope change with the formation of a loop. This confirms that grain boundary or surface effects influence the conduction mechanisms in all samples studied here. In summary, the impedance behavior of different BTO/xYb$_2$O$_3$ modified systems exhibits a complex interaction between resistive and capacitive components, which is largely dependent on frequency, temperature, and stabilizer concentration.

3.10. Cole-Cole fitting analysis and relaxation dynamics

The electrical relaxation analysis of BaTiO$_3$/xYb$_2$O$_3$ ceramics was further investigated over Cole–Cole plots derived from the complex impedance spectra. The Cole–Cole characteristics (ImZ vs ReZ) delivers a powerful method for splitting the electrical contributions arising from grains, grain boundaries, and electrode/interface consequences. Fig. 16 depicts the Cole–Cole fitting outcomes for both temperature variation (20–120 °C) at x = 10 wt% Yb$_2$O$_3$ and x = 0–100 wt%) at 40 °C. Additionally, temperature-dependent

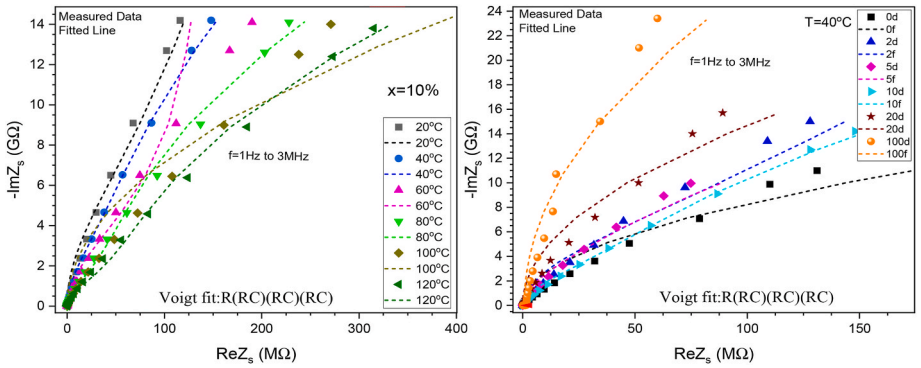

Fig. 16. Cole-Cole fitting analysis of complex impedance of $BaTiO_3/xYb_2O_3$ ceramics for temperature variation at x = 10% **(Left)** and compositional wt.% variations at T = 40 °C **(Right)**.

EEC parameters of $BaTiO_3/xYb_2O_3$ ceramics is reviewed in Table 4 for some temperature ranging from 20 to 120 °C at compositional wt.% of $x = 10\%$. The additive-dependent EEC parameters of $BaTiO_3/xYb_2O_3$ ceramics is summarized in Table 5 for compositional variation of $x = 0$, 2, 5, 10, 20 and 100 wt%) at T = 40 °C. It is noteworthy that the impedance spectra exhibit depressed semicircular arcs rather than precise semicircles, indicating a deviation from ideal Debye relaxation and advocating a distribution of relaxation times within the microstructure. Furthermore, this non-ideal manner is characteristically correlated with heterogeneous conduction pathways and microstructural nonuniformities in ceramics. The Cole–Cole plot fitting was achieved using an EEC model consisting of three parallel RC elements connected in series, representing the grain (R_G–C_G), grain boundary (R_{GB}–C_{GB}), and electrode/interface polarization (R_{IP}–C_{IP}) contributions, together with a series resistance (R_S).

It is also worth noting that the temperature-dependent EEC parameters reveal a strong thermal activation of charge transport. In particular, R_{GB} exhibits significant variation across the concerned temperature range, reaching very high values at intermediate temperatures, indicating that grain boundaries dominate the electrical response under certain conditions. In contrast, R_G remains relatively smaller, inferring that charge transport inside the grains is comparatively easier than across grain boundaries. The capacitance associated with C_{GB}, typically in the pF range, further reinforces the assignment of this contribution to interfacial regions splitting adjacent grains. Moreover, the EEC component (R_{IP}–C_{IP}) resulted from the electrode/interface polarization develops predominantly at low frequencies and exhibits extremely high resistance values, reaching the TΩ range. This conduct reflects the charge accumulations at the electrode–ceramic interface, so becoming particularly pronounced at upraised temperatures due to improved carrier mobility. It is interesting to note that such interfacial polarization is commonly detected in high-resistivity ferroelectric ceramics and contributes substantially to the low-frequency impedance response. It should be noted that the x content-dependence of the Nyquist fitting parameters at 40 °C also offers important intuition into the role of Yb_2O_3 integration. With rising Yb_2O_3 content, notable changes ensue in both R_G and R_{GB}, indicating that the Yb_2O_3 incorporation modifies the charge transport paths and defect chemistry within the $BaTiO_3$ lattice. Additionally, moderate Yb_2O_3 content seems to reduce the grain boundary resistance, implying enhanced electrical conductivity between grains, whereas excessive Yb_2O_3 content guides to an increase in interfacial impedance involvements. Thus, these consequences imply that Yb^{3+} ion incorporation impacts both the defect structure and grain boundary characteristics, thereby impressing the overall electrical relaxation activities of the ceramic system.

The characteristic relaxation time correlated with each EEC component was computed using time constant: $\tau = RC$ where τ signifies the relaxation time, R and C is the resistance, capacitance of each corresponding microstructural region, respectively. The calculated relaxation times expose a strong hierarchy of polarization processes in $BaTiO_3/xYb_2O_3$ ceramics.

Table 4
Temperature-dependent equivalent circuit parameters of $BaTiO_3/xYb_2O_3$ ceramics for some temperature ranging from 20 to 120 °C at compositional wt.% of $x = 10$.

Temp. (°C)	20	40	60	80	100	120
R_G (Ω)	39 m	952 m	46μ	16 m	19 m	220 m
C_G (F)	118 m	704μ	Too big	518μ	Too big	4.5 m
R_{GB} (Ω)	4.8 m	3.8k	2.9 M	829T	5.2 m	302G
C_{GB} (F)	11p	11p	17p	12p	11p	15p
R_{IP} (Ω)	1.24T	1T	0.34T	0.56T	0.53T	0.23T
C_{IP} (F)	3μ	16n	34p	195p	92n	41p
R_S (Ω)	193 M	201k	Too big	303T	Too big	149T

***Footnote:** p = pico; n = nano; μ = micro; m = milli; k = kilo; M = mega; G = giga; T = tera. R_G–C_G, R_{GB}–C_{GB} and R_{IP}–C_{IP} are the ECC parameters representing grain, grain boundary, and electrode/interface polarization involvements, respectively.

Table 5
Composition-dependent equivalent circuit parameters of $BaTiO_3/xYb_2O_3$ ceramics for compositional variation of $x = 0$, 2, 5, 10, 20, and 100 wt%) at T = 40 °C.

x wt. (%)	0	2	5	10	20	100
R_G (Ω)	47k	1.8	121.4	952 m	10.8	369k
C_G (F)	104n	166n	361n	704μ	1.7n	3.7 m
R_{GB} (Ω)	12.7 M	209	39.2	3.8k	4.8	26k
C_{GB} (F)	13p	11p	16p	11p	10p	6p
R_{IP} (Ω)	697G	1.4T	1.0T	1.0T	11T	6.6T
C_{IP} (F)	10 m	1μ	3μ	16n	194μ	3.4n
R_S (Ω)	331T	36T	1.1G	201k	28G	226G

*__Footnote:__ p = pico; n = nano; μ = micro; m = milli; k = kilo; M = mega; G = giga; T = tera. R_G–C_G, R_{GB}–C_{GB} and R_{IP}–C_{IP} are the ECC parameters representing grain, grain boundary, and electrode/interface polarization involvements, respectively.

- **Grain relaxation (10^{-3}–10^{2} s):** The grain relaxation occurs on relatively short timescales compared to interfacial processes and reflects charge transport within semiconducting grains. The moderate temperature dependence suggests thermally activated hopping of localized carriers (possibly involving Ti^{3+}/Ti^{4+} or some states relevant to oxygen vacancy).
- **Grain-boundary relaxation (10^{-14}–10^{4} s):** The grain-boundary relaxation times cover a very widespread range, suggesting that grain boundaries behave as electrically-heterogeneous barrier layers. Hence, such bulky variations are characteristic of $BaTiO_3$-based ceramics demonstrating internal barrier layer capacitor performance, in which insulating grain boundaries isolate more conductive grains.
- **Electrode/interface relaxation (10–10^{12} s):** The enormously long relaxation times associated with the electrode/interface component suggest slow space charge polarization processes. These arise from carrier deposition at the electrode-ceramic interface and dominate the low-frequency impedance response.

Conclusively, the Nyquist impedance analysis reveals that the electrical characteristics of $BaTiO_3$–Yb_2O_3 ceramics is dominated by a multi-scale relaxation process encompassing grain conduction, grain boundary barriers, and electrode/interface polarization. It is evident that the influential role of grain boundaries in the complex impedance spectra emphasizes the strong impact of microstructural heterogeneity on charge transport. Moreover, the modification of impedance parameters with Yb_2O_3 incorporation confirms that RE substitution/addition provides an effective strategy for adapting the defect chemistry and electrical relaxation performance of $BaTiO_3$-based ceramics. It can be concluded that these outcomes determine a clear correlation between substituent or additive-induced microstructural modifications and the subsequent electrical conduction mechanisms, which is critical for optimizing the performance of $BaTiO_3$ ceramics in dielectric and electronic applications.

4. Conclusion

In this work, the structural, morphological, magnetic, electrical, and dielectric evolution of BTO ceramics with high-content Yb_2O_3 additions (2–20 wt%) have been investigated. XRD analysis indicated that while some Yb^{3+} ions entered the BTO lattice, causing an amphoteric A-site/B-site switching mechanism, the solubility limit was quickly reached, leading to the formation of a separate Yb_2O_3 phase. Microstructural analysis via SEM and EDX provided visual and chemical confirmation of these structural findings. Functionally, these structural and morphological changes led to a modification of the magnetic, electrical, and dielectric properties. The magnetic results showed a transition from weak ferromagnetic behavior in pure BTO to a robust ferromagnetic state upon Yb_2O_3 addition, which is mostly due to the bound magnetic polaron (BMP) model, where the electrons are trapped within the oxygen vacancies by the intermediate of exchange coupling between Yb^{3+} ions. $BaTiO_3/xYb_2O_3$ ceramics exhibit strongly substitution-dependent electrical and dielectric performance dominated by defect-mediated charge transport. σ_{AC} follows JPL, confirming a thermally activated hopping mechanism consistent with the CBH model. Both σ_{DC} and E_A analyses reveal that moderate Yb_2O_3 contents (2–10 wt%) enhance charge carrier transport, however higher contents lead to carrier localization and reduced conductivity due to defect blocking and grain boundary influences. The dielectric constant declines significantly with Yb_2O_3 addition, reflecting the evolution toward a composite-like microstructure and repression of long-range ferroelectric polarization. It should also be noted that both dielectric loss and dissipation factor are significantly reduced. Thus, impedance analysis indicates non-Debye relaxation governed by grain boundary and interfacial polarization. It can be concluded that any regulated Yb_2O_3 addition offers an effective route to modify $BaTiO_3$-based ceramics effectively for low-loss dielectric and electronic applications.

CRediT authorship contribution statement

Yassine Slimani: Writing – review & editing, Writing – original draft, Supervision, Resources, Methodology, Investigation, Formal analysis, Conceptualization. **Bayram Ünal:** Writing – review & editing, Writing – original draft, Resources, Investigation, Formal analysis. **Abdulhadi Baykal:** Writing – review & editing, Formal analysis. **Atul Thakur:** Writing – review & editing, Resources, Investigation, Formal analysis.

Declaration of competing interest

The authors declare that they have no known competing financial interests or personal relationships that could have appeared to influence the work reported in this paper.

Acknowledgment

The authors are grateful to the Faculty of Engineering at Duzce University (Turkiye), specifically Mr. Mesut Yildiz and Prof. Ismail Ercan, for their support in conducting the scanning electron microscopy images.

Data availability

Data will be made available on request.

References

[1] R. Li, B. Wang, Y. Zhao, N. Zhang, X. Zhao, Z. Gao, H. Guo, H. Wang, In-situ growth of WO3/Bi2WO6 heterojunctions on carbon fiber cloth: design, morphology modulation and photocatalytic performance, J. Environ. Chem. Eng. 13 (2025) 118926, https://doi.org/10.1016/J.JECE.2025.118926.
[2] F. Jiang, J. Zhang, T. Wang, Z. Chen, J. Liu, Q. Wu, Q. Zhang, X. Zhang, Q. Hu, G. Feng, J. Liu, Y. Yu, Effect of Mg–doping on glaze crystallization inhibition in Ni–doped Al2TiO5 pigments synthesized by non–hydrolytic sol–gel process, Ceram. Int. 52 (2026) 6825–6835, https://doi.org/10.1016/J.CERAMINT.2025.12.432.
[3] W. Zhao, A. Yan, Z. Su, F. Huang, Q. Wang, S. Li, S. Lu, C. Wang, T. Zhang, J. Zhang, Y. Gao, H. Yuan, Multiobjective-optimization MoS2/Cd-ZnIn2S4/CdS composites prepared by in situ structure-tailored technique for high-efficiency hydrogen generation, Small Struct. 5 (2024) 2300569, https://doi.org/10.1002/sstr.202300569.
[4] J. Wang, J. Zhang, G. Cheng, K. Zhang, X. Liu, Performance and mechanism of tetracycline removal by peroxymonosulfate-assisted double Z-scheme LaFeO3/g-C3N4/ZnO heterojunction under visible light drive, Environ. Technol. Innov. 39 (2025) 104302, https://doi.org/10.1016/J.ETI.2025.104302.
[5] Z. Ling, W. Yang, X. Wang, Y. Zhang, J. Jiang, X. Chen, W. Liu, Z. Geng, Y. Peng, Enhanced corrosion resistance of laser-remelted Fe–Cr–B–Mo alloy through interfacial periodic layered structures in liquid aluminum, J. Mater. Res. Technol. 37 (2025) 4717–4731, https://doi.org/10.1016/J.JMRT.2025.07.096.
[6] Q. Sun, L. Yang, F. Hu, C. Liang, H. Wang, J. Qi, Microstructural evolution and kinetics of monoclinic scheelite-type BiVO4-based materials with enhanced color performance, Ceram. Int. 51 (2025) 40414–40430, https://doi.org/10.1016/J.CERAMINT.2025.06.276.
[7] L. Zhang, R. Jing, H. Du, Y. Huang, Q. Hu, Y. Sun, Y. Chang, D. Alikin, X. Wei, W. Cao, V. Shur, S. Zhang, D. Damjanovic, L. Jin, Ultrahigh electrostrictive effect in lead-free ferroelectric ceramics via texture engineering, ACS Appl. Mater. Interfaces 15 (2023) 50265–50274, https://doi.org/10.1021/ACSAMI.3C11432.
[8] A.N. Yadav, D. Habale, M.D. Kirkire, Electronic structure calculations of perovskite type material, AIP Conf. Proc. 3242 (2024), https://doi.org/10.1063/5.0234583/3313520.
[9] T.R. Ponnada, R.K. Nodagala, G. Gurram, Insights into the impact of Y2O3 addition to BaTiO3 on its structural and optical properties, Ceram. Int. 51 (2025) 45128–45140, https://doi.org/10.1016/J.CERAMINT.2025.07.231.
[10] H. Yang, W. Bao, Z. Lu, L. Li, H. Ji, Y. Huang, F. Xu, G. Wang, D. Wang, High-energy storage performance in BaTiO3-based lead-free multilayer ceramic capacitors, J. Mater. Res. 36 (2021) 1285–1294, https://doi.org/10.1557/s43578-020-00093-2.
[11] T. Fang, New insights into the positive temperature coefficient of resistance model of BaTiO 3 -based ceramics, J. Am. Ceram. Soc. 107 (2024) 2048–2051, https://doi.org/10.1111/jace.19589.
[12] C.L. Liu, Q. Du, C. Zhang, J.M. Wu, G. Zhang, Y.S. Shi, Fabrication and properties of BaTiO3 ceramics via digital light processing for piezoelectric energy harvesters, Addit. Manuf. 56 (2022) 102940, https://doi.org/10.1016/J.ADDMA.2022.102940.
[13] A. Nfissi, Y. Ababou, M. Belhajji, S. Sayouri, L. Hajji, M.N. Bennani, Investigation of Ba and Ti sites occupation effects on structural, optical and dielectric properties of sol gel processed Y-doped BaTiO3 ceramics, Opt. Mater. 122 (2021) 111708, https://doi.org/10.1016/J.OPTMAT.2021.111708.
[14] A. Karvounis, F. Timpu, V.V. Vogler-Neuling, R. Savo, R. Grange, Barium titanate nanostructures and thin films for photonics, Adv. Opt. Mater. 8 (2020) 2001249, https://doi.org/10.1002/adom.202001249.
[15] E. Cai, H. Gu, Q. Liu, Electrical property optimization of BaTiO3-based lead-free piezoceramics by chemical doping, J. Am. Ceram. Soc. 106 (2023) 6717–6731, https://doi.org/10.1111/jace.19293.
[16] X. Sang, X. Li, D. Zhang, X. Zhang, H. Wang, S. Li, Improved dielectric properties and energy-storage densities of BaTiO3-doped PVDF composites by heat treatment and surface modification of BaTiO3, J. Phys. D Appl. Phys. 55 (2022) 215501, https://doi.org/10.1088/1361-6463/AC4942.
[17] Y. Huang, C. Zhao, B. Wu, X. Zhang, Grain size effects and structure origin in high-performance BaTiO3-based piezoceramics with large grains, J. Eur. Ceram. Soc. 42 (2022) 2764–2771, https://doi.org/10.1016/J.JEURCERAMSOC.2022.01.026.
[18] Y. Slimani, A. Selmi, E. Hannachi, M.A. Almessiere, A. Baykal, I. Ercan, Impact of ZnO addition on structural, morphological, optical, dielectric and electrical performances of $BaTiO_3$ ceramics, J. Mater. Sci. Mater. Electron. 30 (2019) 9520–9530, https://doi.org/10.1007/s10854-019-01284-2.
[19] T.M. Alfareed, Y. Slimani, M.A. Almessiere, S.E. Shirsath, M. Hassan, M. Nawaz, F.A. Khan, E.A. Al-Suhaimi, A. Baykal, Structure, magnetoelectric, and anticancer activities of core-shell Co0·8Mn0.2R0.02Fe1·98O4@BaTiO3 nanocomposites (R = Ce, Eu, Tb, Tm, or Gd), Ceram. Int. 48 (2022) 14640–14651, https://doi.org/10.1016/J.CERAMINT.2022.01.358.
[20] Y. Slimani, A. Selmi, E. Hannachi, M.A. Almessiere, G. AlFalah, L.F. AlOusi, G. Yasin, M. Iqbal, Study on the addition of SiO2 nanowires to BaTiO3: structure, morphology, electrical and dielectric properties, J. Phys. Chem. Solid. 156 (2021) 110183, https://doi.org/10.1016/j.jpcs.2021.110183.
[21] J. Sun, Y. Li, Research on improving energy storage density and efficiency of dielectric ceramic ferroelectric materials based on BaTiO3 doping with multiple elements, J. Compos. Sci. 7 (2023) 233, https://doi.org/10.3390/jcs7060233.
[22] X. Cheng, Y.C. Zhen, P. Zhao, K. Hui, M. Xiao, L. Guo, Z. Fu, X. Cao, L. Li, X. Wang, Defect mechanisms, oxygen vacancy trapping ability in rare-earth doped BaTiO3 from first-principles and thermodynamics, J. Am. Ceram. Soc. 106 (2023) 5294–5302, https://doi.org/10.1111/JACE.19168.
[23] F.A. Ismail, R.A.M. Osman, M.S. Idris, Review on dielectric properties of rare earth doped barium titanate, AIP Conf. Proc. 1756 (2016), https://doi.org/10.1063/1.4958786/765324.
[24] Y. Meng, K. Liu, X. Zhang, X. Lei, J. Chen, Z. Yang, B. Peng, C. Long, L. Liu, C. Li, Defect engineering in rare-earth-doped BaTiO3 ceramics: route to high-temperature stability of colossal permittivity, J. Am. Ceram. Soc. 105 (2022) 5725–5737, https://doi.org/10.1111/jace.18512.
[25] M. Wang, K. Xue, K. Zhang, L. Li, Dielectric properties of BaTiO3-based ceramics are tuned by defect dipoles and oxygen vacancies under a reducing atmosphere, Ceram. Int. 48 (2022) 22212–22220, https://doi.org/10.1016/J.CERAMINT.2022.04.223.
[26] J.H. Park, E.S. Kim, Effects of MgO and rare-earth oxides (Y2O3, Yb2O3, Dy2O3) on the structural characteristics and electrical properties of BaTiO3, Processes 11 (2023) 3235, https://doi.org/10.3390/pr11113235.
[27] J. Chun, J. Kim, W.W. Lee, E. Jang, Y. Lee, K. Kim, W.J. Choi, W. Jo, W. Kim, B.S. Kang, Effective rare-earth doping on semiconductor behavior for BaTiO3-based automotive MLCCs, Ceram. Int. 50 (2024) 42963–42968, https://doi.org/10.1016/J.CERAMINT.2024.08.142.
[28] V.V. Mitic, Z.S. Nikolic, V.B. Pavlovic, V. Paunovic, M. Miljkovic, B. Jordovic, L. Zivkovic, Influence of rare-earth dopants on barium titanate ceramics microstructure and corresponding electrical properties, J. Am. Ceram. Soc. 93 (2010) 132–137, https://doi.org/10.1111/j.1551-2916.2009.03309.x.

[29] Y. Gao, T. Xie, H. Wang, J. Yang, H. Lin, Effect of Yb2O3 doping on energy storage and dielectric properties of barium titanate based ceramics, J. Mater. Sci. Mater. Electron. 35 (2024) 1719, https://doi.org/10.1007/s10854-024-13470-y.
[30] G. Yao, X. Wang, Y. Yang, L. Li, Effects of Bi2O3 and Yb2O3 on the curie temperature in BaTiO3-based ceramics, J. Am. Ceram. Soc. 93 (2010) 1697–1701, https://doi.org/10.1111/j.1551-2916.2010.03633.x.
[31] Y.H. Song, Y.H. Han, Effects of rare-earth oxides on temperature stability of acceptor-doped BaTiO3, Jpn. J. Appl. Phys. 44 (2005) 6143, https://doi.org/10.1143/JJAP.44.6143.
[32] S.K. Jo, J.S. Park, Y.H. Han, Effects of multi-doping of rare-earth oxides on the microstructure and dielectric properties of BaTiO3, J. Alloys Compd. 501 (2010) 259–264, https://doi.org/10.1016/J.JALLCOM.2010.04.085.
[33] Y. Slimani, H. Erdemi, A. Baykal, A. Thakur, M. Shariq, M.A. Almessiere, Tailoring the dielectric behavior of BaTiO3 via incorporation of vanadium-substituted barium hexaferrite and thermal effects, Nano-Struct. Nano-Objects 43 (2025) 101539, https://doi.org/10.1016/J.NANOSO.2025.101539.
[34] K. Zhang, L. Li, M. Wang, W. Luo, Charge compensation in rare earth doped BaTiO3-based ceramics sintered in reducing atmosphere, Ceram. Int. 46 (2020) 25881–25887, https://doi.org/10.1016/J.CERAMINT.2020.07.072.
[35] S. Wang, S. Zhang, X. Zhou, B. Li, Z. Chen, Effect of sintering atmospheres on the microstructure and dielectric properties of Yb/Mg co-doped BaTiO3 ceramics, Mater. Lett. 59 (2005) 2457–2460, https://doi.org/10.1016/J.MATLET.2005.03.016.
[36] A. Jain, A.K. Panwar, Synergetic effect of rare-earths doping on the microstructural and electrical properties of Sr and Ca co-doped BaTiO3 nanoparticles, Ceram. Int. 46 (2020) 10270–10278, https://doi.org/10.1016/J.CERAMINT.2020.01.020.
[37] S. Sarraf, S. Singh, Enhanced electrocaloric response and energy storage performance of Li-substituted BaTiO3 ceramics, J. Am. Ceram. Soc. 105 (2022) 6196–6206, https://doi.org/10.1111/jace.18579.
[38] N. Gadwala, M. Hashim, K.M. Batoo, M. Hadi, M.M. Ismail, S.J. Salih, T.A. Nhlapo, S.E. Shirsath, Effect of Nd-substitution on structural and electrical properties of bismuth nano-ferrites, Micro Nanostruct. 207 (2025) 208261, https://doi.org/10.1016/J.MICRNA.2025.208261.
[39] A. Kumari, K. Kumari, F. Ahmed, A. Alshoaibi, P.A. Alvi, S. Dalela, M.M. Ahmad, R.N. Aljawfi, P. Dua, A. Vij, S. Kumar, Influence of Sm doping on structural, ferroelectric, electrical, optical and magnetic properties of BaTiO3, Vacuum 184 (2021) 109872, https://doi.org/10.1016/J.VACUUM.2020.109872.
[40] S.K.S. Patel, S.K. Chauhan, A. Kumar, S. Kumar Srivastav, Structural and magnetic properties of Dy3+-doped BaTiO3 nanorods: a study of the tetragonal-to-cubic phase transition and emergent diluted magnetism, J. Magn. Magn Mater. 636 (2025) 173658, https://doi.org/10.1016/J.JMMM.2025.173658.
[41] S. Fuentes, N. Barraza, E. Veloso, R. Villarroel, J. Llanos, Effects of Eu substitution on luminescent and magnetic properties of BaTiO3 nanomaterials, J. Alloys Compd. 569 (2013) 52–57, https://doi.org/10.1016/J.JALLCOM.2013.02.127.
[42] B.B. Straumal, A.A. Mazilkin, S.G. Protasova, A.A. Myatiev, P.B. Straumal, G. Schütz, P.A. van Aken, E. Goering, B. Baretzky, Magnetization study of nanograined pure and Mn-doped ZnO films: formation of a ferromagnetic grain-boundary foam, Phys. Rev. B 79 (2009) 205206, https://doi.org/10.1103/PhysRevB.79.205206.
[43] Y. Slimani, B. Ünal, A. Baykal, M.A. Almessiere, A. Thakur, M. Shariq, Investigation of electrical and dielectric properties of BaTiO3-based composite systems incorporated with various amounts of Co0.8Mn0.1Ni0.1Fe1.9Ce0.1O4, J. Mater. Sci. Mater. Electron. 35 (2024) 927, https://doi.org/10.1007/s10854-024-12690-6.
[44] Y. Slimani, B. Unal, E. Hannachi, A. Selmi, M.A. Almessiere, M. Nawaz, A. Baykal, I. Ercan, M. Yildiz, Frequency and dc bias voltage dependent dielectric properties and electrical conductivity of BaTiO3SrTiO3/(SiO2)x nanocomposites, Ceram. Int. 45 (2019) 11989–12000, https://doi.org/10.1016/J.CERAMINT.2019.03.092.
[45] Y. Slimani, H. Erdemi, A. Baykal, M.A. Almessiere, A. Thakur, K.M. Batoo, Synergistic impact of metal/semiconductor (Co@Co3O4) core-shell nanostructures on the structure, electrical, and dielectric properties of BaTiO3-based composites, J. Phys. Chem. Solid. 195 (2024) 112292, https://doi.org/10.1016/J.JPCS.2024.112292.
[46] A.K. Jonscher, Dielectric relaxation in solids, J. Phys. D Appl. Phys. 32 (1999) R57, https://doi.org/10.1088/0022-3727/32/14/201.
[47] Y. Wang, J. Li, Y. Zhou, Z. Gao, W. Zhu, L. Liu, Interfacial defect mediated charge carrier trapping and recombination dynamics in TiO2-based nanoheterojunctions, J. Alloys Compd. 872 (2021) 159592, https://doi.org/10.1016/J.JALLCOM.2021.159592.
[48] M.A. El-Naggar, M.A. Mousa, S.M. Reda, M.M. Emara, The electrical conductivity mechanisms and dielectric properties of multiphase Co-synthesized CuV2O6–MnV2O6, Metall. Mater. Trans. B 56 (2025) 141–153, https://doi.org/10.1007/s11663-024-03328-3.
[49] D.Y. Gui, C.H. Wang, The microstructure and dielectric properties of Yb2O3 doped 0.92BaTiO3 - 0.08(Na0.5Bi0.5)TiO3 relaxor ceramics, Mater. Sci. Eng., B 291 (2023) 116386, https://doi.org/10.1016/J.MSEB.2023.116386.
[50] C. Martínez-Morales, P. Arellanes-Lozada, J.L. Rodríguez, A. Romero-Serrano, D. González-García, Analysis of the electrical conductivity and activation energies of bismuth titanate (Bi4Ti3O12), Heliyon 10 (2024) e39523, https://doi.org/10.1016/J.HELIYON.2024.E39523.
[51] H.-J. Hsu, K.H. Yang, H.-I. Hsiang, Effects of CaZrO3 doping on the oxygen vacancy formation and dielectric properties of BaTiO3 ceramics sintered in a reducing atmosphere, J. Mater. Sci. Mater. Electron. 36 (2025) 335, https://doi.org/10.1007/s10854-025-14392-z.
[52] X. Ma, Y. Huang, R. Jing, D. Alikin, X. Wei, Y. Yan, L. Jin, Rare-earth element doped barium titanate-based ceramics exhibiting ultra-wide temperature span electrocaloric effect, Ceram. Int. 50 (2024) 12341–12350, https://doi.org/10.1016/J.CERAMINT.2024.01.139.
[53] G. Jin, J. Chen, J. Cheng, U. Ulfa, Y. Iriani, K. Kusumandari, Microstructure, morphology, and dielectric properties of Ba1-xLaxTiO3 with variation mole concentration of lanthanum by Co-Precipitation method, IOP Conf. Ser. Mater. Sci. Eng. 1096 (2021) 012138, https://doi.org/10.1088/1757-899X/1096/1/012138.
[54] S.A. Bhat, I.A. Itoo, R. Mushtaq, M. Ikram, Enhanced multifunctionality in Nd- and Zn-doped BaTiO3: structural, optical, dielectric, and catalytic insights for sustainable wastewater treatment, J. Mater. Sci. Mater. Electron. (36) (2025) 507, https://doi.org/10.1007/S10854-025-14572-X, 2025 369.
[55] Q. Sun, Q. Gu, K. Zhu, R. Jin, J. Liu, J. Wang, J. Qiu, Crystalline structure, defect chemistry and room temperature colossal permittivity of Nd-doped barium titanate, Sci. Rep. 7 (2017) 42274, https://doi.org/10.1038/SREP42274.
[56] Q. Liu, J. Liu, D. Lu, T. Li, W. Zheng, Dense Sm and Mn Co-Doped BaTiO3 ceramics with high permittivity, Materials 12 (2019) 678, https://doi.org/10.3390/ma12040678.
[57] Z. Cai, L. Cheng, X. Huang, P. Wang, X. Fu, J. Yang, R. Sun, Z. Fu, X. Cao, L. Zhang, Thermal stability of dielectric properties of Dy-doped BaTiO3 for application in the ultra-thin multilayer ceramic capacitors, Ceram. Int. 50 (2024) 53744–53752, https://doi.org/10.1016/J.CERAMINT.2024.10.227.
[58] C.H. Wu, J.P. Chu, S.F. Wang, Microstructure and electrical properties of Ho-doped BaTiO 3-sputtered films, J. Appl. Phys. 98 (2005) 26109, https://doi.org/10.1063/1.1984083/349757.
[59] V. Paunović, V.V. Mitić, M. Đorđević, M. Marjanović, L. Kocić, Electrical characteristics of Er doped BaTiO3 ceramics, Sci. Sinter. 49 (2017) 129–137, https://doi.org/10.2298/SOS1702129P.
[60] Z. Chen, H. Xinyou, G. Hao, G. Chunhua, Effect of Y2O3 and Dy2O3 on dielectric properties of Ba0.7 Sr0.3 TiO3 series capacitor ceramics, J. Rare Earths 25 (2007) 197–200, https://doi.org/10.1016/S1002-0721(07)60468-2.
[61] A.I. Ali, S. Abu Alrub, R.K. Hussein, J.Y. Son, A.B. El Basaty, The impact of Gd on structural, morphology, dielectric behavior of BaTiO3, Sci. Rep. (15) (2025) 33735, https://doi.org/10.1038/s41598-025-93014-4, 2025 151.
[62] Z. Hasan, M.D. Faysal, J.S. Jahan, L. Mollah, P. Das, D.K. Das, N.A. Jahan, Effect of Ce doping on the multifunctional properties of $BaTiO_3$: from bandgap engineering to mechanical stability, Next Mater. 9 (2025) 101133, https://doi.org/10.1016/J.NXMATE.2025.101133.
[63] W. Li, X. He, Y. Liu, O. V'yunov, D. Pang, Dielectric, ferroelectric, and high-temperature strain behavior of rare Earth Ce-Doped 0.67BiFeO3–0.33BaTiO3 lead-free ferroelectric ceramics, ACS Appl. Electron. Mater. 5 (2023) 6974–6984, https://doi.org/10.1021/ACSAELM.3C01361.
[64] V.V. Mitic, V. Paunovic, D. Mancic, L. Kocic, L. Zivkovic, V.B. Pavlovic, Dielectric properties of BaTiO3 doped with Er2O3 and Yb2O3 based on intergranular contacts model, in: Ceram. Trans., American Ceramic Society, 2009, pp. 137–144, https://doi.org/10.1002/9780470528990.ch16.
[65] D.Y. Gui, X.Y. Ma, H.D. Yuan, C.H. Wang, Mn- and Yb-Doped BaTiO3-(Na0.5Bi0.5)TiO3 ferroelectric Relaxor with low dielectric loss, Materials 16 (2023) 2229, https://doi.org/10.3390/ma16062229.

[66] L. Liu, Z. Mei, A. Tang, A. Azarov, A. Kuznetsov, Q.K. Xue, X. Du, Oxygen vacancies: the origin of n-type conductivity in ZnO, Phys. Rev. B 93 (2016) 235305, https://doi.org/10.1103/PhysRevB.93.235305.
[67] F. Wu, T.J. Smart, J. Xu, Y. Ping, Carrier recombination mechanism at defects in wide band gap two-dimensional materials from first principles, Phys. Rev. B 100 (2019) 081407, https://doi.org/10.1103/PhysRevB.100.081407.
[68] P. Liang, Z. Yang, X. Chao, Improved dielectric properties and grain boundary response in neodymium-doped Y2/3Cu3Ti4O12 ceramics, J. Alloys Compd. 678 (2016) 273–283, https://doi.org/10.1016/J.JALLCOM.2016.03.294.
[69] I. Kovač, M. Mužević, M.V. Pajtler, I. Lukačević, Charge carrier dynamics across the metal oxide/BaTiO3 interfaces toward photovoltaic applications from the theoretical perspective, Surf. Interfaces 39 (2023) 102974, https://doi.org/10.1016/J.SURFIN.2023.102974.
[70] Y. Slimani, B. Unal, M.A. Almessiere, E. Hannachi, G. Yasin, A. Baykal, I. Ercan, Role of WO3 nanoparticles in electrical and dielectric properties of BaTiO3–SrTiO3 ceramics, J. Mater. Sci. Mater. Electron. 31 (2020) 7786–7797, https://doi.org/10.1007/s10854-020-03317-7.
[71] Y. Slimani, B. Ünal, A. Baykal, M.A. Almessiere, A. Thakur, K.M. Batoo, Unraveling the dielectric and electrical properties of binary BaTiO3/Ba0.98Ca0.01Mg0.01Fe12O19 composites, J. Phys. Chem. Solid. 191 (2024) 112047, https://doi.org/10.1016/J.JPCS.2024.112047.
[72] D.W. Hahn, Y.H. Han, Electrical properties of Yb-Doped BaTiO3, Jpn. J. Appl. Phys. 48 (2009) 111406, https://doi.org/10.1143/JJAP.48.111406.
[73] S. Zhang, S. Wang, X. Zhou, B. Li, Z. Chen, Influence of 3d-elements on dielectric properties of BaTiO3 ceramics, J. Mater. Sci. Mater. Electron. 16 (2005) 669–672, https://doi.org/10.1007/s10854-005-3744-8.
[74] D.W. Hahn, S.B. Sohn, Y.H. Han, Effects of rare-earth oxides on time-dependent dielectric properties of Mn-Doped BaTiO3, Jpn. J. Appl. Phys. 48 (2009) 031404, https://doi.org/10.1143/JJAP.48.031404.
[75] B.P. Das, P.K. Mahapatra, R.N.P. Choudhary, Effect of Sm3+ ions on structural, dielectric, and electrical properties of Pb(SnTi)O3 ceramics, J. Mater. Sci. Mater. Electron. 15 (2004) 107–114, https://doi.org/10.1023/B:JMSE.0000005386.88365.19.